Effects of flow loop compressible volume position on system instabilities during flow boiling in micro-channel heat sinks

Jeongmin Lee, V.S. Devahdhanush, Steven J. Darges, Issam Mudawar[1],*

Purdue University Boiling and Two-Phase Flow Laboratory (PU-BTPFL), School of Mechanical Engineering, Purdue University, 585 Purdue Mall, West Lafayette, IN 47907, USA

ARTICLE INFO

ABSTRACT

Much of published literature addressing flow instabilities in thermal management systems employing micro-channel modules has focused on the instability characteristics of the module alone, and far fewer studies have aimed at understanding the relationship between these characteristics and the compressible volume in the flow loop external to the module. From a practical point of view, developers of micro-channel thermal management systems for many modern applications are in pursuit of practical remedies that would greatly mitigate instabilities and their impact on cooling performance. The present study experimentally examines the effects of compressible volume location in a closed pump-driven flow loop designed to deliver FC-72 to a micro-channel test module having 38 channels with 315-μm hydraulic diameter. Three accumulator locations are investigated: upstream of the test module, downstream of the test module, and between the condenser and the pump. Both high-frequency temporal parameter data and high-speed video records are analyzed for ranges of mass velocity and heat flux, with inlet subcooling held constant at ~14.5 °C. Pressure Drop Oscillation (PDO) is shown to dominate when the accumulator is situated upstream, whereas Parallel Channel Instability (PCI) is dominant for the other two locations. PDO shows severe pressure oscillations across the micro-channel heat sink, with rapid bubble growth and confinement, elongated bubble expansion in both directions, flow stagnation, and flow reversal (including vapor backflow to the inlet plenum) constituting the principal sequence of events characterizing the instability. Spectral analysis of pressure signals is performed using Fast Fourier Transform, which shows PDO extending the inlet pressure fluctuations with the same dominant frequency to other upstream flow loop components, with higher amplitudes closer to the pump exit. From a practical system operation point of view, throttling the flow upstream of the heat sink effectively eliminates PDO but renders PCI dominant, and placing the accumulator in the liquid flow segment of the loop between the condenser and the pump ensures the most stable operation.

© 2022 Elsevier Ltd. All rights reserved.

1. Introduction

1.1. Thermal management challenges of high-heat-flux applications

Recent years have witnessed unprecedented pursuit of automation/electrification in a broad range of industrial applications. Almost all international automakers are transitioning toward electric vehicles for the various benefits they offer over conventional internal-combustion-engine vehicles. Metaverse, the new platform for a virtual world, is very close to implementation and expected to lead to enormous increases in cloud data server loads. Increased shift to cloud-based services and big data would also lead to fur-

ther increases in satellite communication. These technological advances on a global scale have one thing in common: increased power levels and more compact footprints leading to highly power-dense devices, which require more effective and reliable thermal management systems to handle the massive amounts of waste heat generated.

In the past, single-phase cooling satisfactorily achieved the set thermal guidelines, but a fundamental transition to two-phase cooling has become inevitable for many state-of-the-art applications. By utilizing both sensible and latent heats, two-phase schemes yield one to two orders of magnitude higher heat transfer coefficients compared to single-phase liquid schemes, and hence are especially beneficial for cooling both high-heat-flux devices and aerospace systems, where high heat fluxes need to be dissipated while keeping the cooling system small and lightweight. Two-phase cooling has been adopted using a variety of thermal

Nomenclature

A	amplitude
Bo	boiling number, q''_w/Gh_{fg}
c_p	specific heat at constant pressure
D_h	hydraulic diameter
F	force
F_{back}	backward vapor momentum
$F_{forward}$	forward liquid momentum
f	frequency
G	mass velocity
H_{ch}	channel height
h	enthalpy
h_{fg}	latent heat of vaporization
L	channel length
$L_{sp,f}$	length of upstream liquid region
$\dot{m}$	mass flowrate of heat sink
N_{ch}	number of channels in heat sink
N_{pch}	phase change number, $(h_f - h_{in})/h_{fg} \cdot (v_g - v_f)/v_f$
N_{sub}	subcooling number, $Q/\dot{m}h_{fg} \cdot (v_g - v_f)/v_f$
P	pressure
ΔP	pressure drop, P_{in} - P_{out}
Q	electric power input
Q_v	volumetric flow rate
ΔQ_g	vapor generation rate
q''	heat flux
R	instability parameter, $Q/(2Ah_{fg}G) \cdot \sqrt{\rho_f/\rho_g}$
Re	Reynolds number, GD_h/μ
T	temperature
ΔT_{sub}	fluid subcooling, T_{sat} - T_f
t	time
v	specific volume
W_{ch}	channel width
W_w	half-width of copper wall between channels
x_e	thermodynamic equilibrium quality, $(h - h_f)/h_{fg}$
z	streamwise coordinate

Greek symbols

ρ	density

Subscripts

avg	averaged
ch	channel
f	saturated liquid; single-phase liquid; bulk fluid
fo	liquid only
g	saturated vapor
in	inlet
max	maximum
out	outlet
sat	saturated
sp	single-phase
tc	thermocouple
z	axial local

Acronyms

CHF	critical heat flux
DWO	density wave oscillation
FDB	fully developed boiling
OFI	onset of flow instability
PCI	parallel channel instability
PDB	partial developed boiling
PDO	pressure drop oscillation

management schemes. Capillary-driven devices, such as heat pipes [1], loop heat pipes [2,3], capillary pumped loops [4], and capil-

lary thermosyphons [5], all operating without a mechanical pump, are relatively simple and compact, but with heat dissipation rates smaller than those required by high-heat-flux devices. Pool boiling [6] and falling films [7,8] provide improved cooling performances, but are very dependent on body force and hence suitable for neither reduced gravity environments nor variable heated surface orientations. Flow boiling in macro-channel(s) [9,10] is quite effective due to reliance on faster fluid motion, but less attractive in terms of system size and weight. Jet impingement cooling [11], spray cooling [12], micro-channel heat sinks [13–15], and hybrid jet impingement/micro-channel heat sinks [16] have been deemed the most effective for high-heat-flux devices by Mudawar [17]. Jet impingement is capable of managing very high heat fluxes, especially within the impingement zone, while operating with relatively small pressure drop. However, they suffer from system limitations stemming from their high flow rate requirement, large surface temperature gradients, and potential flow instabilities resulting from collision of wall jets emanating from neighboring impingement zones. Sprays are capable of uniformly cooling large surfaces if droplet breakup downstream of the spray nozzle is well controlled. However, these systems are complicated to setup due to cooling performance being dependent on a large number of design parameters including, but not limited to, flow rate, coolant temperature, nozzle pressure drop, cone angle, mean droplet size, droplet trajectories, nozzle-to-surface distance, and heated surface shape and size.

Two phase micro-channel heat sinks, arguably the most popular scheme for cooling high-heat-flux devices, are capable of dissipating large amounts of heat with relatively uniform surface temperatures and low flow rates while remaining compliant with the small volume requirements of modern electronic devices [17]. Compared to their macro-channel counterpart, micro-channel heat sinks handily resist the effects of orientation encountered in flow boiling [18]. However, compared to mini-/macro-channels, micro-channels experience a relatively large increase in pressure drop upon the initiation of boiling [19,20], which is however smaller than the total pressure drop of the entire thermal management system. This can lead to significant thermophysical property variations resulting in choking at much lower flow velocities than single-phase flows [9,21–23]. Two-phase micro-channel heat sinks, similar to macro-channel flows, are prone to flow instabilities, albeit with their own unique manifestation and consequences [24]. When using a micro-channel heat sink, the first design objective is to sustain operation within the nucleate boiling dominant regime to enable high heat transfer coefficients, h. The convective boiling dominant regime, on the other hand, has relatively low h and induces intermittent/partial dryout, which may result in system failure [25]. Within micro-channels, h is strongly dependent on applied heat flux where bubbly/slug flows are dominant but weakly dependent on heat flux at higher thermal equilibrium qualities and even shows appreciable degradation due to rapid reduction in the annular liquid film's momentum and increased periods of intermittent dryout. The other main design objective is to suppress flow instabilities. Bubble confinement within micro-channels and their growth in the axial direction [26] cause flow fluctuations, flow reversal, partial dryout, and even premature critical heat flux (CHF) in extreme cases [27]. Other design considerations include avoiding (i) normal CHF and (ii) the combined effects of compressibility, flashing, and two-phase choking, which are more probable with smaller channel diameters [9].

1.2. Two-phase instabilities and effects of compressible volume

Two-phase instabilities are broadly categorized into two: static and dynamic. Static instabilities refer to single excursions of flow condition from one unstable operating state to another. On the

other hand, dynamic instabilities are associated with periodic operation between marginally unstable operating states and are sustained by feedback between flow rate, pressure drop, and density changes, the latter being dependent on the rate of vapor production. Some examples of the former are Ledinegg instability and CHF, and the latter Density Wave Oscillation (DWO), Pressure Drop Oscillation (PDO), and Parallel Channel Instability (PCI). These instabilities are dependent on a multitude of parameters such as:

(i) Geometry – length-to-hydraulic-diameter ratio, number of channels, inlet/outlet plenum configurations,
(ii) Operating conditions – inlet pressure, channel inclination, and
(iii) Boundary conditions – inlet subcooling (or quality), mass flowrate, and heat input.

With all channels sharing inlet and outlet plenums, flow maldistribution can greatly contribute to instabilities in micro-channel heat sinks due to likelihood of dynamic pressure variations among channels.

Both PDO and PCI were well illustrated by Qu and Mudawar [28] in their experiments with water flowing through a micro-channel heat sink containing 21 parallel 231 × 713 μm channels. PDO was associated with simultaneous boiling boundary (axial location separating single- and two-phase regions) oscillation, moving back and forth in all channels between the inlet and outlet, often involving vapor backflow into the inlet plenum. Experiments involving PDO also featured severe high-frequency oscillations of inlet and outlet pressures resulting from interactions between the vapor generated within channels and the system stiffness, the latter being dictated mostly by the presence of a compressible volume in the flow loop. On the other hand, PCI involved relatively mild inlet and outlet pressure fluctuations and were observed replacing PDO when adding system stiffness such as incorporating a throttling valve upstream of the heat sink. Unlike PDO, the boiling boundary in each channel moved in an apparently random manner and the flow regimes varied from bubbly to slug at low heat fluxes and from slug to annular at medium/high heat fluxes.

It is known that flow oscillations can manifest if a sufficiently large compressible volume is placed upstream of a heated section due to the interaction between flow excursions within the heat sink and system compressibility [29–32]. An accumulator, fluid reservoir, surge tank, inlet plenum (header) or even a large length-to-diameter channel can serve as a compressible volume and cause flow fluctuations when positioned upstream of a boiling module. Following are key aspects of PDO [33,34] which are captured in Fig. 1 [34] in terms of the interrelationship between the system's internal characteristic curve and the pump's external characteristic curve:

(i) The boundary conditions of the heated section (boiling module) would correspond to the dotted curve given by valve coefficient, K_1, and constant pressures, P_0 and P_{out}.
(ii) Because of flow perturbation, an initial operating point, which is at the intersection of the two characteristic curves, on the negative-slope portion of the system's curve would move operation to peak point D, causing an increase in the amount of generated vapor.
(iii) With the pump now capable of delivering higher flow rate than that corresponding to point D, the system undergoes an unstable excursion from point D to single-phase point A.
(iv) At point A, with the system now demanding a flow rate exceeding the pump's capability, system operation moves from point A to a minimum point B and a decompression in the surge tank occurs.
(v) With point B still at a higher flow rate than the pump's, a second unstable excursion occurs, shifting operation from low quality point B to a high-quality point C.

(vi) With the system's flow rate now lower than the pump's, operation moves along the system's curve up to point D and a compression in the surge tank occurs, completing a full cycle.
(vii) Therefore, a perturbation at any point along the negative-slope region of the system's curve can trigger flow oscillation cycles traversing D-A-B-C-D.

Like Ledinegg instability, which manifests when the slope of the system demand curve is steeper than that of the pump's pressure-flowrate curve (external characteristic curve) in the negative-slope portion of the internal characteristic curve, PDO manifests in the negative-slope portion with a compressible volume present [24].

Table 1 provides a summary of studies [28,35–44] concerning flow boiling instabilities, especially PDO, in micro-channel heat sinks along with the respective compressible volume position. Yu et al. [36] reported that a large-volume-pressurizer situated upstream of their test module led to surge tank compressibility and flow excursion effects which caused flow instability in a rectangular mini-channel. In Tuo and Hrnjak's [39] experiments with a refrigerant tank and large-sized inlet header, a multi-micro-channel evaporator experienced boiling fluctuations and periodic reversed flow at low frequencies. By supplying liquid nitrogen to their test section from a surge tank upstream, Qi et al. [37] reported long period and large amplitude oscillations of mass flux, pressure drop, and wall temperature corresponding to the onset of nucleate boiling (ONB) during flow boiling in an open flow loop. Oscillations in mass flux and pressure drop were 180° out-of-phase, a key feature of PDOs. Cheng et al. [42] investigated the characteristics of PDO in a closed natural-circulation loop of water by changing the pressurizer's position. Moving the compressible volume to the downstream of the test module helped mitigate PDO occurrence, but mass flow rate and pressure drop still fluctuated due to DWOs. Almost all prior researchers who observed PDO employed flow loops having the compressible volume placed upstream of the test module (and downstream of the pump in closed loops), which is why the effects of the compressible volume position on PDO warrant further study.

It is apparent that PCI manifests in micro-channel heat sinks due to interactions between neighboring channels. DWOs in each individual channel, which manifest as growth, confinement, and axial expansion of bubbles in a channel, cause flow fluctuations that culminate in a dynamic and oscillatory mode of flow instability. Due to the presence of multiple flow paths, interactions between neighboring channels may result in either (i) flow rates in individual channels to fluctuate while the total flow rate is maintained constant or (ii) the total flow rate to oscillate as individual channel flow rates remain equal yet oscillating in-phase. Following are key aspects of PCI: (i) initiated by DWOs within individual channels leading to interactions among channels, (ii) amplified by a decrease in mass flow rate and/or increase in heat input, (iii) associated with vapor backflow into the inlet plenum at high heat fluxes, (iv) frequency and amplitude dominated by heat flux (generally increasing with increases in heat flux) and mass flow rate, (v) frequency and amplitude also governed by operating conditions (*e.g.*, system pressure, subcooling) as well as liquid length within channels upstream of confined bubble formation, and (vi) generally associated with high frequencies and low amplitudes.

Prior studies [45–54] addressing PCI in micro-channel heat sinks are summarized in Table 2 with the respective compressible volume positions identified. Lee et al. [45] investigated the frequency and amplitude of pressure fluctuations during PCI in a large-*L/D* parallel micro-channel heat sink with a reservoir downstream of the condenser. They compared high-speed-video results of vapor backflow into the inlet plenum and found it to closely align with the frequency of inlet pressure fluctuations obtained via Fourier analysis. The same authors [55], not listed in Table 2, iden-
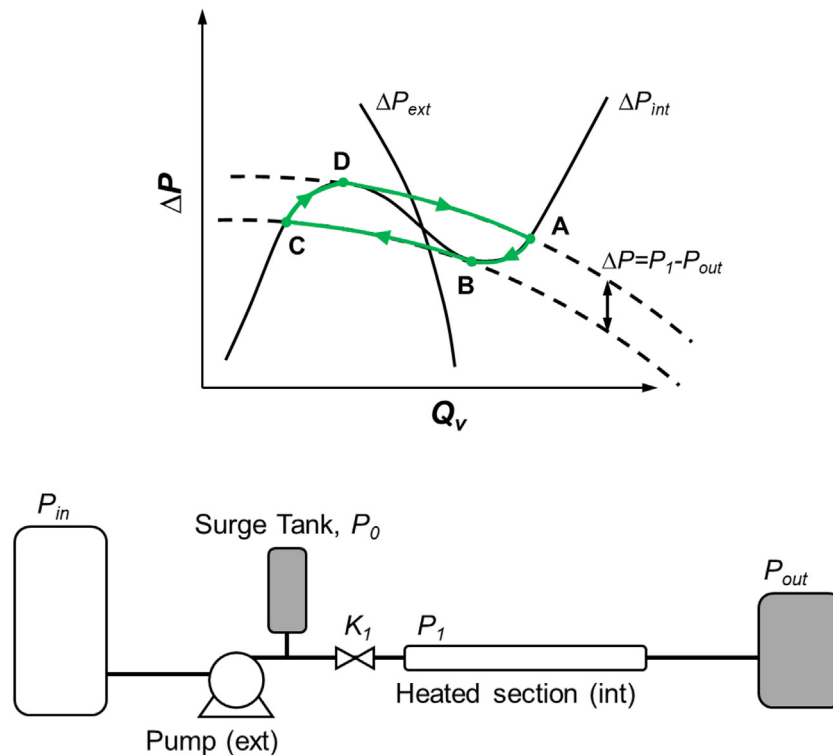
Fig. 1. Schematic of systems' internal characteristic curve and pump's external characteristic curve and limit cycle of pressure drop oscillation (PDO) (adapted from [34]).

tified a dominant charge transition instability (CTI) which featured large amplitude, long period, and in-phase fluctuations of mass velocity and pressure drop. CTI was associated with pressure oscillations at the condenser inlet, outlet, and reservoir resulting in liquid level oscillations in the reservoir. Chang and Pan [46] observed flow boiling in a micro-channel heat sink with a collecting container downstream of the test section. They varied both flow rate and heat flux and found PCI to manifest in most of their cases. Reversed flow into the inlet plenum occurred when the difference between the minimum and the maximum instantaneous pressure drop exceeded 6 kPa. Cases with lesser pressure drop fluctuations were deemed as stable or experiencing mild oscillations, in which, bubbly, slug, and annular two-phase flow patterns appeared sequentially in the direction of flow. Xu et al. [51] conducted experiments to measure the onset of flow instability (OFI) in a micro-channel heat sink with a downstream reservoir. They observed OFI when the outlet fluid approached saturation conditions, but still remained slightly subcooled. Upon reaching OFI, small bubbles were observed exiting the channel and coalescing in the outlet plenum. The authors observed large amplitude/long period oscillations (LALPO), small amplitude/short period oscillations (SASPO), and thermal oscillations, which accompanied the former two. LALPO occurred at higher inlet subcoolings and featured alternating periods of liquid and vapor dominance in the channel. They were always superimposed upon SASPO, which occurred as the boiling boundary oscillated within the channel.

From the aforementioned studies, it is apparent that the compressible volume and its location greatly influences the stability of the system. Compressible volumes are required in two-phase loops to account for volume changes caused by phase change and prevent flow excursions such as Ledinegg instability [20]. The compressible volume is typically positioned near the loop components in which phase change occurs, such as, the single-phase region upstream of the heater (to set the reference pressure near the inlet), the two-phase region immediately downstream of the

heater (to account for vapor production within the heater), or the single-phase region downstream of the condenser (to set a minimum system pressure upstream of the pump). However, as concluded in a recent comprehensive review on two-phase instabilities by O'Neill and Mudawar [24], the exact influence of the compressible volume's position on system stability is not well understood.

1.3. Objectives of present study

The present study explores the effects of compressible volume position in a closed flow loop on occurrence of two-phase instabilities during flow boiling of FC-72 in a micro-channel heat sink. The heat sink contains 38 straight parallel rectangular channels of hydraulic diameter 316 μm and a large length-to-diameter ratio. An accumulator is used as the compressible volume. Three different accumulator positions are investigated, upstream and downstream of the test module (directly interacting with compressibility of the vapor produced in the heat sink) and between the condenser and the pump (with only liquid entering and leaving the accumulator). Key objectives are summarized as follows:

(1) Examine fluctuations of the heat sink's inlet and outlet pressures in response to changes in compressible volume position along the flow loop. Identify the type of dominant instabilities and their characteristics.
(2) Using high-speed video, determine flow regime transitions along the channels and dynamic behavior of vapor-backflow-induced PDO and PCI.
(3) Explore the effects of mass velocity and heat flux (at constant inlet subcooling) on frequency and amplitude of system instabilities for each accumulator position.
(4) Assess the ability of stability maps in demarcating stable from unstable operation.

Table 1

Prior studies on pressure drop oscillation (PDO) in micro-channel heat sinks and corresponding compressible volume position(s).

Author(s)	Compressible volume | Position	Operating conditions	Channel geometry	Remarks
Qu & Mudawar [28]	Thermal circulating bath | Upstream Reservoir | Upstream (bypass loop), downstream	$G = 134.9$–400.1 kg/m^2 s $q''_b = 0$–2400 kW/m^2	$L = 44.8$ mm $W_{ch} \times H_{ch} = 0.231 \times 0.712$ mm^2 $D_h = 0.349$ mm $N_{ch} = 21$	R M CL Water
Wu & Cheng [35]	Surge tank | Upstream Container | Downstream	$G = 112$–146 kg/m^2 s $q''_b = 135$–226 kW/m^2	$L = 30$ mm $D_h = 0.186$ mm $N_{ch} = 8$	TZ M OP Water
Yu et al. [36]	Pressurizer | Upstream	$Q_v = 0.1$–0.5 m^3/h $Q = 0$–9 kW	$L = 1000$ mm $W_{ch} \times H_{ch} = 40 \times 2$ mm^2 $D_h = 3.809$ mm $N_{ch} = 1$	R S CL Water
Qi et al. [37]	Surge tank | Upstream	$G = 440$–3000 kg/m^2 s $q''_b = 50.9$–213.9 kW/m^2 $P_{in} = 180$–920 kPa $T_{in} = 78.2$–79.8 K	$L_{h,1} = 120$ mm $L_{h,2} = 250$ mm $D_h = 0.531, 0.834, 1.042, 1.931$ mm $N_{ch} = 1$	C S OP Nitrogen
Kuang et al. [38]	Buffer tank | Upstream Storage tank | Downstream	For ammonia $G = 124$ kg/m^2 s $q''_b = 18.75$ kW/m^2 For water $G = 170$ kg/m^2 s $q''_b = 129$ kW/m^2	$L = 250$ mm $W_{ch} \times H_{ch} = 1 \times 1.1$ mm^2 $N_{ch} = 4$	R M CL/OP Ammonia Water
Tuo & Hrnjak [39]	Gas tank | Upstream, downstream (bypass loop)	$Q_v == 0.233$ m^3/s $q''_b = 8.37$–10.8 kW/m^2	$L = 260$ mm $D_h = 1$ mm $N_{ch} = 25$	C M CL R134a
Guo et al. [40]	Surge tank | Upstream	$G = 150$–2500 kg/m^2 s $q''_b = 0$–540 kW/m^2 $P_{sys} = 0.5$–3.5 MPa	$L = 6448$ mm $D_h == 15$ mm $N_{ch} = 1$	C S CL Water
Ding et al. [41]	Surge tank | Upstream	$G = 75$–1050 kg/m^2 s $q''_b = 0$–100 kW/m^2	$L = 1060$ mm $D_h == 10.9$ mm $N_{ch} = 1$	C S CL R-11
Cheng et al. [42]	Pressurizer | Upstream, downstream (controlled by valves)	$G \approx 150$–290 kg/m^2 s $q''_b = 10$–280 kW/m^2 $P_{in} = 0.3$–0.8 MPa $x_{e,out} = -0.008$–0.012	$L_h = 800$ mm $D_h = 6$ mm $N_{ch} = 3 \times 3$	C M CL Water
Park et al. [43]	Expansion tank | Upstream Main tank | Downstream	$G = 400$–1000 kg/m^2 s $q''_b = 35$ kW/m^2	$L = 2035$ mm $D_h = 5$ mm $N_{ch} = 1$	C S CL R134a
Grzybowski & Mosdorf [44]	Surge tank | Upstream	$G = 159.2$ kg/m^2 s $Q = 46$ W	$L_h = 100$ mm $D_h = 1$ mm $N_{ch} = 1$	C S OP Water

R: rectangular, TZ: trapezoidal, C: circular.
S: single channel, M: multiple channels.
CL: closed loop, OP: open loop.

2. Experimental methods

2.1. Test module

To investigate the dynamic behavior and corresponding instabilities of flow boiling in a micro-channel heat sink, the present test module was designed to enable simultaneous temporal thermal measurements and high-speed-video photography. As portrayed in the 3D-CAD exploded view in Fig. 2(a), the module has 5 main components: cover plate, housing, micro-channel heat sink, insulating layer, and bottom support plate. The heat sink contains 38 parallel micro-channels of width $W_{ch} = 203$ μm and height $H_{ch} = 713$ μm, machined into an oxygen-free copper slab of width $W = 20$ mm, length $L = 90$ mm, and height 5 mm. The thickness of the wall separating neighboring channels is 254 μm and the edge walls 1.444 mm. The heat sink is inserted into an insulating G-10 fiberglass-plastic housing, within which are machined the inlet and outlet plenums of rough dimensions 30 mm × 15 mm × 22 mm.

The design of both plenums is intended to promote uniform and symmetrical flow distribution. The heat sink is held in place and its bottom insulated using another layer of G-10. A transparent cover plate made of polycarbonate plastic seals the top of the heat sink and allows for optical access. All the module layers are placed on an aluminum support plate and clamped together using threaded rods and fasteners. To prevent fluid leaks, O-rings are used both in grooves milled around the perimeter of the heat sink and between the housing and cover plate.

An exploded view of the assembly of heaters to the underside of the copper heat sink is shown in Fig. 2(b). A 3 × 7 array of 169-Ω thick-film resistors of width 5.2 mm and length 11.6 mm is soldered to the underside. To ensure uniform heat distribution, all resistors are connected in parallel and electric power input is controlled by a single variable autotransformer. Spread evenly in-between the resistors are a 4 × 8 array of 5.0-mm-diameter, 2.5-mm-deep holes for insertion of type-E thermocouples. Thermal contact resistance is minimized by securing the thermocou-

Table 2

Prior studies on Parallel Channel Instability (PCI) in micro-channel heat sinks and corresponding compressible volume position(s).

Author(s)	Compressible volume | Position	Operating conditions	Channel geometry	Remark
Lee et al. [45]	Reservoir | Downstream	G = 75.9–436.6 kg/m^2 s q''_b = 2.7–29.6 kW/m^2	L = 609.6 mm $W_{ch} \times H_{ch}$ = 1 × 1 mm^2 D_h = 1 mm N_{ch} = 100	R M CL R134a
Chang & Pan [46]	Collecting container | Downstream	G = 22–110 kg/m^2 s q''_b = 7.86–95.5 kW/m^2	L = 20 mm $W_{ch} \times H_{ch}$ = 0.0994 × 0.0763 mm^2 D_h = 0.0863 mm N_{ch} = 15	R M OP Water
Muwanga & MacDonald [47]	Supply tank | Downstream	G = 91–228 kg/m^2 s q''_b = 0–100 kW/m^2	L = 16 mm $W_{ch} \times H_{ch}$ = 0.269 × 0.283 mm^2 D_h = 0.2758 mm N_{ch} = 45	R M CL Water
Wang et al. [48]	Collecting container | Downstream Pressure tank | Upstream	G = 142.3–311.2 kg/m^2 s (M) 950–3523.2 kg/m^2 s (S) q''_b = 226.9–496.8 kW/m^2	L = 30 mm D_h = 0.186 mm N_{ch} = 2	TZ S, M CL Water
Hetsroni et al. [49]	Reservoir | Downstream	G = 32–200 kg/m^2 s q''_b = 100–270 kW/m^2	L = 15 mm D_h = 0.1, 0.13, 0.22 mm N_{ch} = 5	T M OP Water Ethanol
Balasubramanian & Kandlikar [50]	Collecting container | Downstream Pressure tank | Upstream	G = 112–120 kg/m^2 s q''_b = 208–316 kW/m^2	L = 63.5 mm $W_{ch} \times H_{ch}$ = 0.990 × 0.207 mm^2 D_h = 0.333 mm N_{ch} = 6	R M OP Water
Xu et al. [51]	Reservoir | Downstream	G = 20–1200 kg/m^2 s Q = 100–450 W	L = 50 mm $W_{ch} \times H_{ch}$ = 0.3 × 0.8 mm^2 D_h = 0.436 mm N_{ch} = 26	R M CL Water
Lu & Pan [52]	Collecting container | Downstream	G = 99–297 kg/m^2 s q''_b = 171–324 kW/m^2	L = 26 mm $W_{ch} \times H_{ch}$ = 0.100–0.560 × 0.076 mm^2 D_h = 0.12 mm (mean) N_{ch} = 10	C M CL Water
Wang et al. [53]	Supply tank | Downstream	G = 9.3–37.3 kg/m^2 s q''_b = 0–500 kW/m^2 P_{in} = 23–30 MPa	L = 4000 mm $W_{ch} \times H_{ch}$ = 25 × 3 mm^2 D_h = 5.357 mm N_{ch} = 2	R M CL Water
Bogojevic et al. [54]	Main tank | Downstream	G = 400–1000 kg/m^2 s q''_b = 35 kW/m^2	L = 2035 mm D_h = 5 mm N_{ch} = 40	C M CL R134a

R: rectangular, TZ: trapezoidal, C: circular, T: triangle
S: single channel, M: multiple channels.
CL: closed loop, OP: open loop.

ple beads in place using thermal epoxy, followed by mechanical strengthening by application of another layer of high-strength epoxy atop the thermal epoxy.

2.2. Closed two-phase flow loop

A schematic diagram of the closed two-phase flow loop used to maintain the desired operating conditions is illustrated in Fig. 2(c). FC-72, a thermally and chemically stable dielectric fluid, is used as coolant and circulated through the loop using a variable-speed magnetically-driven gear pump. A pressure relief valve is provided for safety, 10-micron filter to remove any fluid impurities, and turbine flow meter to measure the flow rate. The desired subcooling and/or flow quality at the inlet of the test module is achieved using a preheater, wherein heat is added using another variable auto-transformer. A condenser is placed downstream of the test module to convert the two-phase mixture back to low-temperature liquid. A membrane contactor is installed on a bypass path to the main loop and used to remove any non-condensable gases from FC-72 prior to performing experiments.

A nitrogen-pressurized accumulator compensates not only to volume changes of FC-72, but also helps maintain a stable reference pressure point in the loop. This Flexicraft-Hydropad-HY-12 accumulator is made of stainless steel 316 and contains metal bellows that shrink or expand depending on the pressure and volume on either side of them. The volume of its fluid side (fluid displacement) is 1.97 L, volume of its gas side (nominal gas capacity) is 3.27 L, and maximum operating pressure is 200 psi. A transparent flexible tubing is used to connect the accumulator to the main loop to help monitor the inflow/outflow of fluid. Three accumulator positions are investigated in this study: (1) downstream of the test module, (2) upstream of the test module, and (3) between the condenser and the pump, by manually re-connecting the same accumulator's flexible tubing to different locations of the main flow loop prior to starting different sets of experiments (and not during the experiments to avoid disturbing the flow stability/instability).

2.3. Instrumentation, measurement accuracy, and experimental procedure

The two-phase interfacial physics within the micro-channels is visualized using a high-speed camera system with the aid of fiber-optic lighting and high-density LEDs. The camera is moved to different regions atop the test module and high-speed videos are recorded; a resolution of 1024 × 1024 at 500 fps is used for the entrance and exit regions and 512 × 256 at 10,000 fps for the
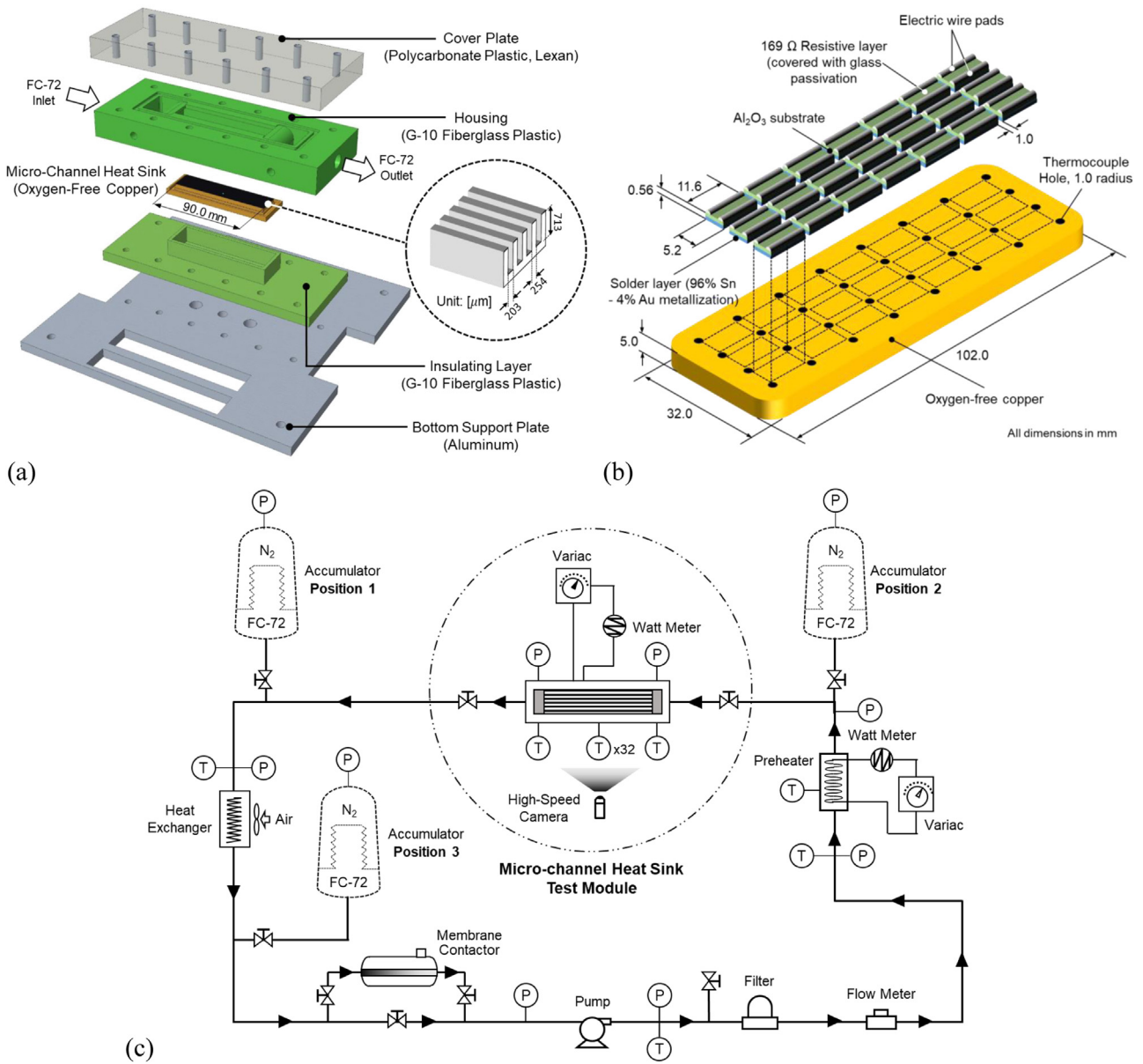
Fig. 2. (a) Exploded view of micro-channel heat sink test module with key dimensions of flow channels, (b) layout of thick-film resistors and thermocouple insertion holes, and (c) schematic of flow loop.

other sub-regions along the length of the test section. High shutter speeds are required to capture the dynamic behavior at high flow rates.

Fluid pressures and temperatures are measured at the inlet and outlet plenums of the test module using Honeywell-SJTE pressure transducers and type-E thermocouples, respectively. The 32 type-E substrate thermocouples and 2 type-E fluid thermocouples within the test module have an accuracy of ±0.4 °C. The preheater's temperature is measured using a type-K thermocouple of accuracy ±0.6 °C and the coolant temperature at multiple locations of the flow loop using type-T thermocouples of accuracy ±0.45 °C. Pressure measurements both within the test module and at multiple locations in the flow loop are made with an accuracy of ±0.06%. Flow rate is measured by the turbine flow meter with ±0.1% accuracy. Output signals from all sensors are recorded in a NI-SCXI-100 data acquisition system and monitored in LabVIEW software. The temporal data (temperatures, pressures, flow rate, and heater power) are sampled at a frequency of 200 Hz, allowing for high-

fidelity transient analysis of flow instabilities. The propagated uncertainties were estimated by the root sum square method and found to be a maximum of ±2.076 W, ±8.136 kPa, and ±0.310 for measured power, pressure drop, and inlet equilibrium quality, respectively, during severe instability.

The operating conditions are set to achieve constant inlet subcooling and/or quality and mass flow rate during the course of experimentation, both before supplying electric power to the heaters and after the onset of instabilities. Since instabilities tend to gradually decrease the average mass flow rate and subcooling, both pump speed and preheater power input are carefully controlled to reestablish the set operating conditions; it is noted that, due to the difficulty in maintaining constant conditions throughout an entire instability period, this is done only if the flow rate varies by ±10% and subcooling by ±3 °C. However, as soon as the system becomes hydrodynamically unstable with severe oscillations, no manual changes are made so as to capture the true instability behavior. Experiments are conducted by keeping both the mass

flow rate and subcooling constant, and increasing the heat flux from zero to a maximum, which is dictated by the wall temperature reaching 120 °C. Experiments are repeated for different mass flow rates and the three accumulator locations. The accumulator pressure at each position is controlled to achieve identical inlet pressures at the beginning before heat flux increment for identical inlet saturation temperatures.

OFI is determined by observation of both temporal fluctuations in hydrodynamic parameters and visual flow reversal. Thermodynamic fluctuations were not induced by any of the instabilities observed in this study and hence are not used to identify the flow state. More details on the experimental methods and heat loss are available in the authors' prior study [56].

The inlet thermodynamic equilibrium quality is determined as

$$x_{e,in} = \frac{h_{in} - h_f}{h_{fg}} = -\frac{c_{p,f}(T_{sat} - T_{in})}{h_{fg}},$$ (1)

where $c_{p,f}$, T_{sat}, and h_{fg} are based on the measured inlet pressure and T_{in} is the measured inlet temperature. The outlet quality is calculated by applying an energy balance over the entire module as

$$x_{e,out} = x_{e,in} + \frac{Q}{\dot{m} h_{fg}},$$ (2)

where Q is the power input to the heat sink. Q is obtained from an iterative scheme adopted in previous micro-channel heat sink studies [57]. During the first iteration, local wall temperatures are calculated considering 1-D conduction from the substrate thermocouple to the wetted surface, and heat transfer coefficients via fin analysis. Initial heat loss is assumed to be the difference between the electrical power input and the fluid's sensible-heat increase. A finite element model is constructed encapsulating the test section, housing, cover plate, and insulation. Averaged heat transfer coefficient, wall temperature, fluid temperature, and natural convection from the entire housing are adopted as boundary conditions in the model to estimate heat loss. Subsequent iterations consider an updated value of power input based on the heat loss from the previous iteration, and updated values of average heat transfer coefficient, wall temperature, and fluid temperature are calculated.

The experimental setup has been validated by comparing the experimental values of average single-phase liquid heat transfer coefficient, $h_{sp,f,avg}$, with the theoretically-predicted values for fully developed laminar flows [58]. For all 7 single-phase experiments at different flow rates and heat fluxes, experimental $h_{sp,f,avg}$ was almost constant, matching expected trends, and very close to the predicted values with a mean absolute error of 3.51%.

Instability data is carefully investigated over 60 s out of the entire period after reaching quasi-steady state, and important variables are time-averaged. Ranges of operating conditions tested in this study are as follows: inlet thermodynamic equilibrium quality of $x_{e,in} = -0.27 – -0.15$, mass velocity of $G = 242.2–935.8$ kg/m^2 s, inlet pressure of $P_{in} = 132.5–269.0$ kPa, inlet subcooling of $\Delta T_{sub,in} = 11.0–18.0$ °C, and outlet thermodynamic equilibrium quality of $x_{e,out} = -0.05–1.03$. Negative inlet qualities are representative of the fluid entering the test module in subcooled state.

A finite value of inlet subcooling is essential to determine both the single-phase liquid length and the subcooled boiling dominant length for two-phase flow instabilities. Flow instability is the result of force imbalance on the liquid-vapor interface at the upstream end of a growing bubble; flow reversal occurs when the backwards evaporation momentum due to rapid bubble growth is larger than the forwards liquid inertia. This is especially pronounced in micro-channel heat sinks, where bubble confinement occurs far upstream due to their small channel diameter. Flow reversal could also be caused when the rate of vapor generation at the upstream interface is more than the rate of liquid supply to individual channels

from the inlet header [59]. Thus, a dominant single-phase liquid length enables easy investigation of flow instabilities. This indicates that flow instabilities in micro-channel heat sinks, especially severe pressure drop oscillations (sPDO), are easily observed during subcooled flow boiling operation.

3. Results and discussion

3.1. High-speed images of vapor backflow into inlet plenum and severe PDO-induced flow regime transitions

Representative time-sequential images of periodic vapor backflow into the inlet plenum due to PDO (with accumulator situated upstream of test module) and PCI (with accumulator situated downstream) are depicted in Fig. 3(a) and (b), respectively. In the former, a key feature of the PDO instability is the boiling boundary between the liquid and two-phase regions moving upstream and causing aggressive simultaneous vapor backflow from all channels into the inlet plenum. Note how at 34 ms an appreciable part of the inlet plenum is filled with vapor and pure liquid is limited to the very left, close to the plenum's inlet. Vapor continues to backflow until 86 ms when pressure buildup causes a vapor surge through the channels. All vapor is quickly released from the inlet plenum and in less than 10 ms, only liquid is present. By analyzing the high-speed videos, it is observed that each PDO cycle (defined as the period between the instants the plenum is filled with liquid right after a complete vapor surge) takes ~100 ms. Enlarged images of a single channel at t_1 and t_2 (corresponding to the white arrows in Fig. 3(a)) are included in Fig. 3(c), from which new bubble generation and rapid bubble growth are observed in a 14-ms period. Note that this occurs during the PDO period with no vapor backflow. The bubbles rapidly grow to almost fill the channel cross-section, and then proceed to extend both upstream and downstream, leading to vapor backflow at t_3.

The image sequence in Fig. 3(b) corresponding to PCI depicts a dynamic backflow pattern and flow maldistribution between channels. Unlike the regular temporal pattern of backflow during PDO, PCI is characterized by a rather random behavior of vapor backflow alternating between the upper and lower sets of channels. This interaction between channels results in flow rate oscillations in each individual channel even when the total heat-sink flow rate is held constant. The time period of these events varies between 0.070 and 112.0 ms, indicative of non-uniformity of the cycle. Vapor backflow from the middle set of channels accompanied by vapor stagnation is observed every ~270 ms on average. Vapor backflow induced by PCI is also observed when the accumulator is situated between the condenser and the pump but is negligible enough to not be clearly captured by the video camera.

These dynamic flow behaviors within the inlet plenum, in addition to the parameters discussed later, are a direct result of transient flow patterns within the micro-channels. To better understand this, a single micro-channel is focused upon, and transient flow patterns are captured at two different axial locations (upstream and downstream within the micro-channel heat sinks); those for a representative PDO-dominant operating condition of $G = 252.1$ kg/m^2 and $q'' = 40.9$ kW/m^2 are shown in Fig. 4. The individual images at each location are listed in the same order of flow pattern fluctuations as shown in Fig. 3(a): (i) vapor surge, (ii) inlet plenum filled with liquid (liquid surge), (iii) vapor backflow, and (iv) vapor stagnation. Note how it is difficult to identify dominant flow patterns during instabilities due to the highly complex interfaces, which are further blurred due to flow acceleration. Fig. 4(a) and (b) includes subfigures of dominant flow regimes within a PDO periodic cycle at $z = 12$ and 63 mm, which are organized with the specified time interval.
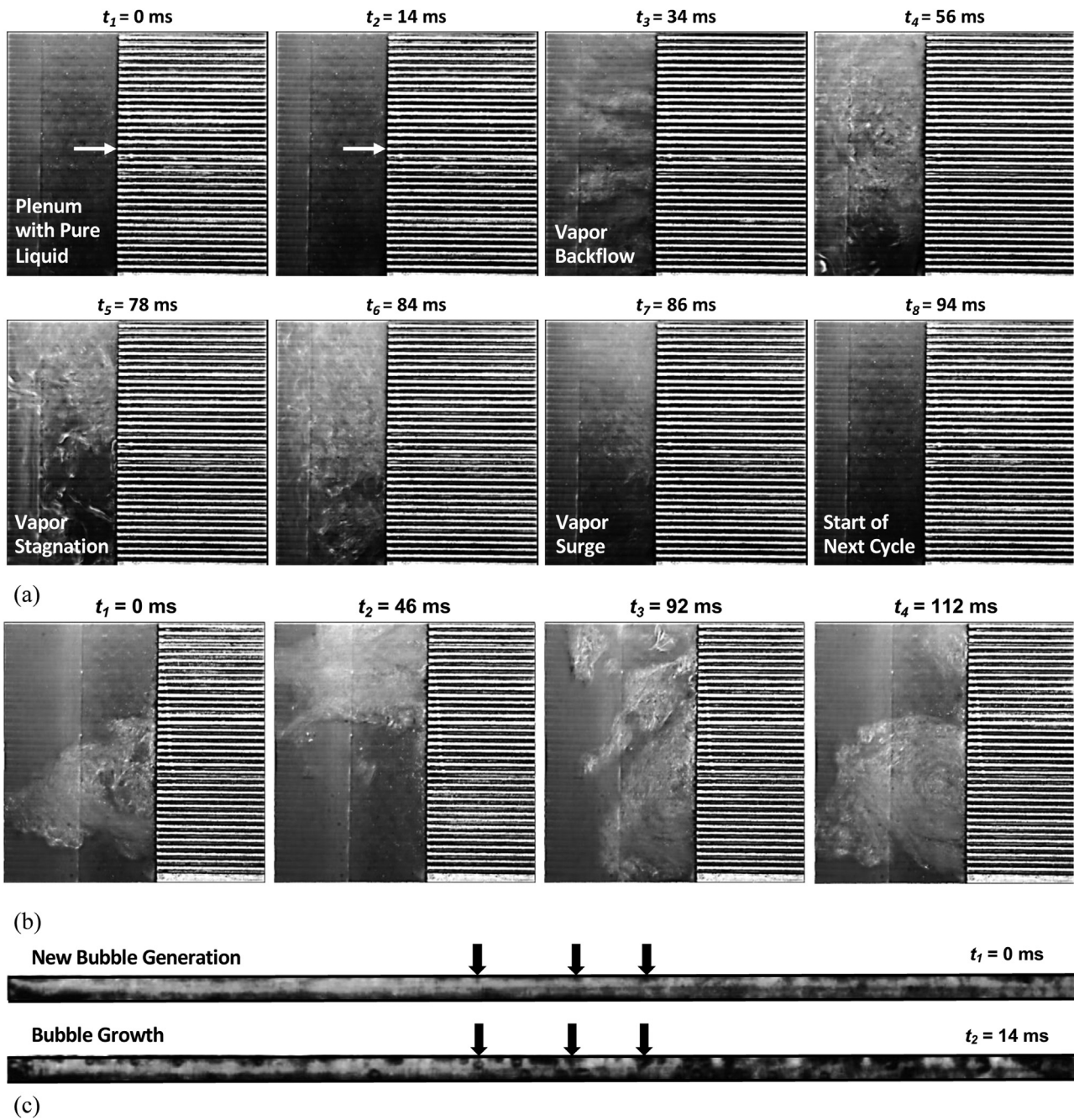
(a)

(b)

(c)

Fig. 3. Time-sequential images of (a) Pressure Drop Oscillations (PDOs) and (b) Parallel Channel Instability (PCI). (c) Enlarged images of a single micro-channel corresponding to the first two time-frames, t_1 and t_2, of the PDOs in (a).

At the upstream location of $z = 12$ mm with a corresponding averaged $x_e = -0.11$, the flow patterns identified are churn, bubbly/slug, annular, misty, and dryout. Churn flow is observed during the ∼10-ms period of vapor surge from the inlet plenum. Afterwards, when liquid enters the channel, new bubbles are generated which grow rapidly causing a bubbly/slug flow situation where the flow varies between bubbly flow (characterized by numerous small bubbles) and slug flow (characterized by elongated bubbles with smaller liquid portions in between). The elongated bubbles are seen to be the cause of onset of flow reversal due to their expansion in both directions within the channel. Longer residence time at the same location and increased void fraction cause the elongated bubbles to transition to annular flow, whose interface sometimes becomes wavy. The interface gradually evaporates until

very fine droplets formed by breakup of the film culminate in a misty flow. Further heating evaporates even the mist causing temporal dryout, which is observed until fresh liquid enters the channel. A similar cycle of flow patterns is also observed at the further downstream location of $z = 30$ mm (which is not presented in this figure), except for the slightly higher average quality. The average fluid temperature at this location is expected to have reached T_{sat}.

The transient flow patterns observed at 63 mm (where the averaged fluid state is saturated) are simpler compared to those observed upstream. Three primary regimes are identified: churn, annular, and dryout. Churn flow is observed during the vapor and liquid surge periods, with the flow being very turbulent. Discrete vapor bubbles interact with one another and coalesce forming distorted vapor structures. Annular flow and dryout are observed dur-
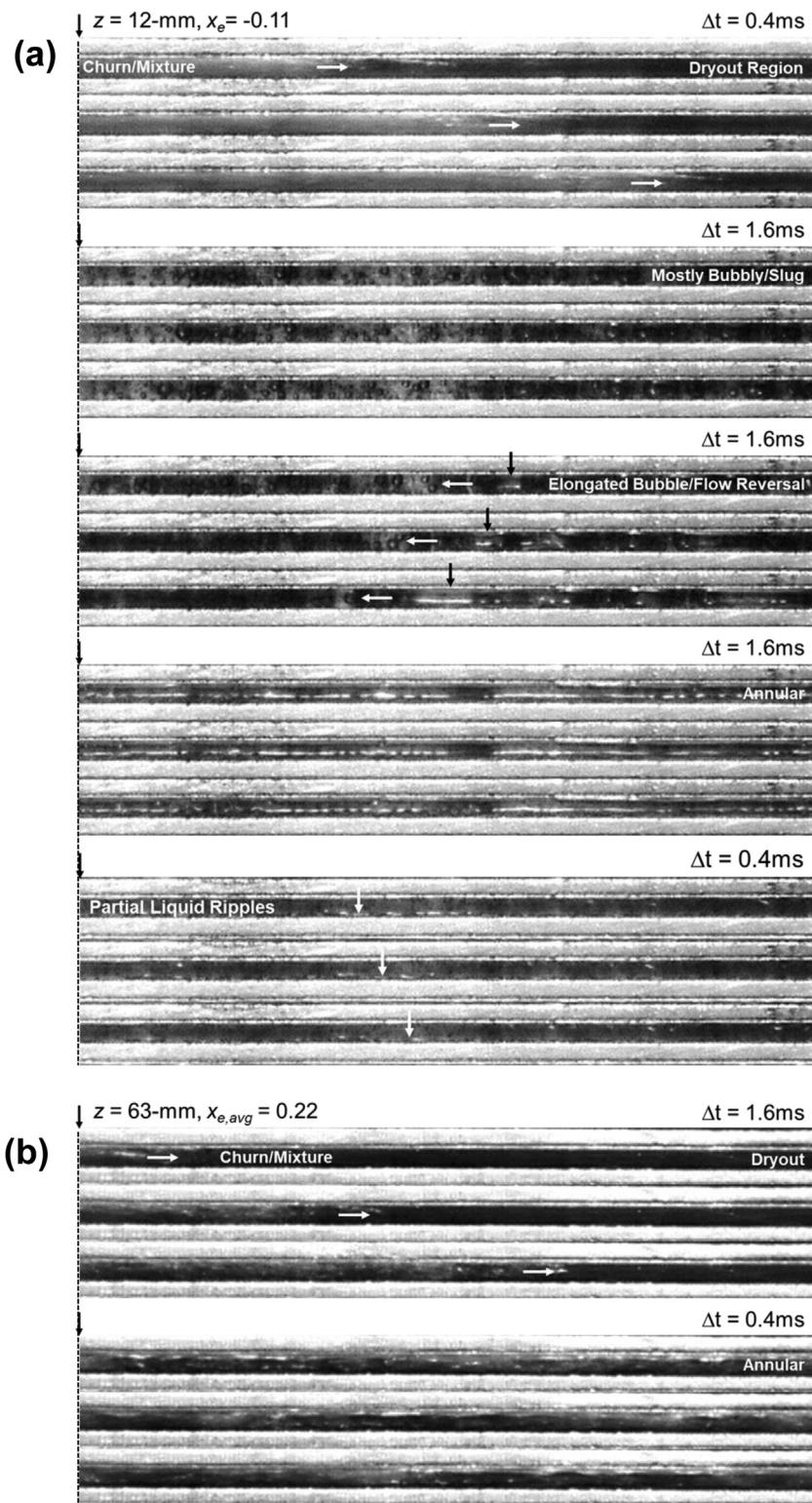
Fig. 4. Transient flow regime variations at two different axial locations of (a) z = 12-mm and (b) z = 63-mm during pressure drop oscillation (PDO) for G = 252.1 kg/m^2 s and q'' = 40.9 kW/m^2 with the accumulator situated upstream of heat sink.

ing the vapor backflow and vapor stagnation periods when the flow slows and liquid supply is greatly diminished.

These transient flow pattern variations all along the channels within a single periodic cycle cause corresponding pressure fluctuations due to transient variations of both boiling boundary location and flow rate, which will be discussed in the upcoming sections.

3.2. Hydrodynamic characteristics for different compressible volume positions

3.2.1. Temporal records of mass velocity and test module pressures

Five-second temporal records of the test module's inlet and outlet pressures and mass velocity are shown in Fig. 5 for different
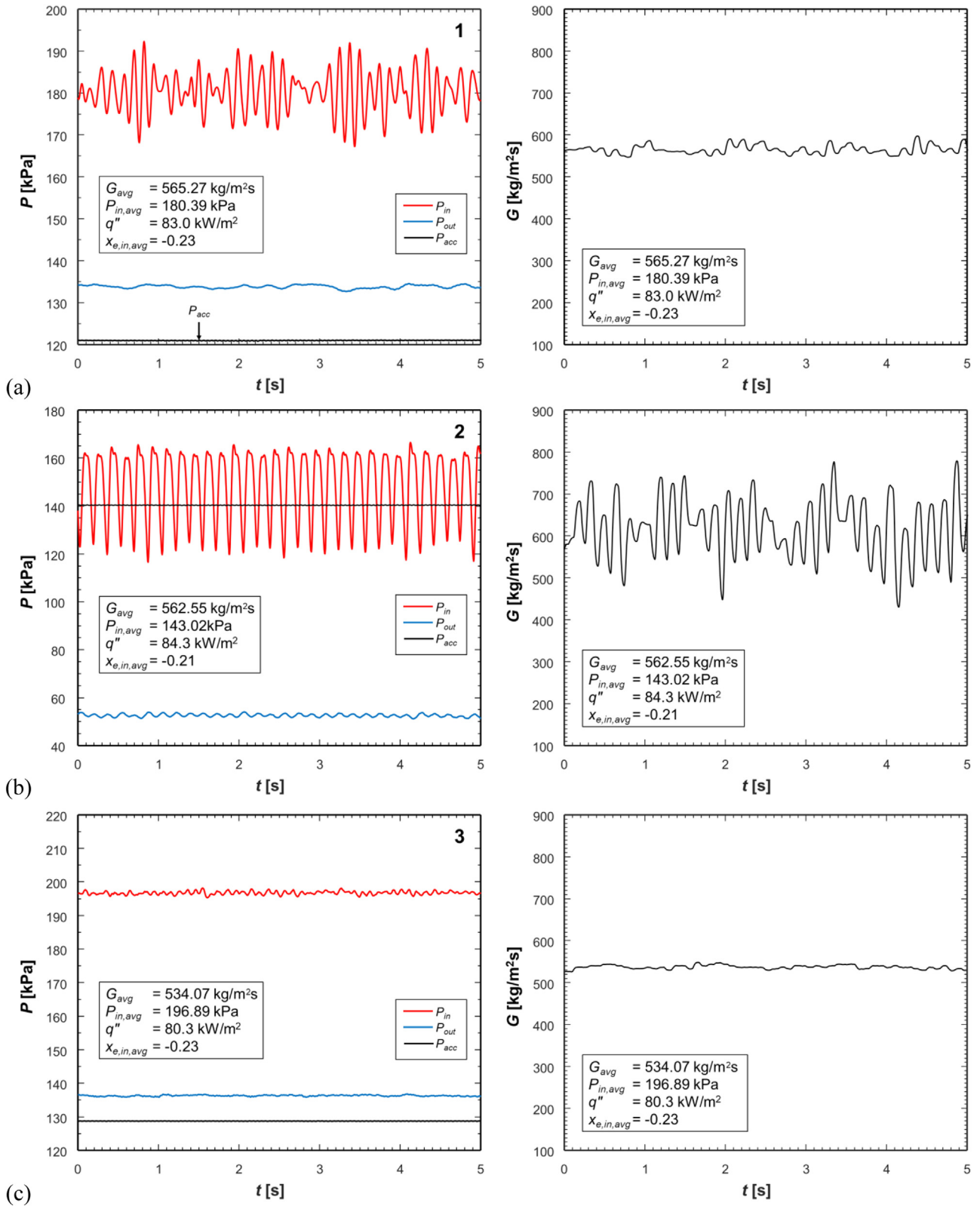
Fig. 5. Temporal records of test module inlet/outlet and accumulator pressures and mass velocity during two-phase instabilities with the accumulator positioned at (a) 1 = downstream of test module, (b) 2 = upstream of test module, and (c) 3 = between condenser and pump.

accumulator positions on the flow loop. The time-averaged operating conditions are similar for all 3 locations with $G = 534.07$–565.27 kg/m² s, $q'' = 80.3$–84.3 kW/m², and $x_{e,in} = -0.21$ – -0.23. For the accumulator position downstream of the test module, Fig. 5(a), PCI induces large inlet pressure fluctuations with a peak-to-peak of ~20 kPa, while the outlet pressure is relatively stable due to the accumulator situated close by. Although P_{in} fluctuations seem rather random, they are superimposed with various modes. G fluctuates to a small extent, confirming that the total flow rate is maintained fairly constant with PCI, even though the flow rate in each channel varies drastically.

In Fig. 5(b), with the accumulator positioned upstream of the test module, PDO induces severe inlet pressure and small outlet pressure oscillations. The amplitude of P_{in} oscillations is the largest of all instabilities observed in this study and is almost double that induced by PCI for similar operating conditions. These consistent and regular oscillations in turn cause G to fluctuate considerably in the range of ~440–790 kg/m² s. Interestingly, in accordance with prior studies [28], PDO promotes both P_{in} and P_{out} to oscillate in-phase with a much longer period than those observed in present study. The amplitude of P_{out} oscillations in this current study is much smaller than those of P_{in} and the period is shorter than PDOs generally reported in the literature [28,40,60]. This could be due to the (i) high quality in the outlet plenum resulting from dryout occurring in the downstream region of the heat sink, (ii) boiling boundary moving back and forth in the upstream region of the heat sink (which would transmit backward evaporation momentum through the liquid phase), and (iii) relatively small test module (as any compressible volume, such as inlet plenum, will affect the amplitude and period [43]).

When the accumulator is positioned between the condenser and the pump, all 3 parameters (P_{in}, P_{out}, G) are very stable as shown in Fig. 5(c). This may be associated with increased system stiffness due to reduced influence of compressible volume as most of the vapor is fully condensed back to liquid in the condenser and the only compressible volumes in the system are in the inlet and outlet plenums. It is visually confirmed that, at this accumulator position, only liquid enters or exits the accumulator as opposed to the position downstream of the test module, where vapor bubbles enter the accumulator upon PCI occurrence.

Also notice the accumulator pressures are temporally stable with the amplitudes of pressure oscillations being negligible (less than 1 kPa), working well to set a reference pressure. As already described in Section 2.3, the accumulator pressure is adjusted to set a constant test-module inlet pressure at the beginning of all cases. When the accumulator is placed upstream of the test module, the inlet pressure is well maintained to be close to the reference pressure set by the accumulator. In this scenario, as heat flux is increased, outlet pressure decreases as a result of increased ΔP. On the other hand, when the accumulator is placed downstream of the test module (or placed between the condenser and the pump), the outlet pressure is well maintained. In these scenarios, as heat flux is increased, inlet pressure increases. Hence, the saturation temperatures with the accumulator situated upstream is lower than that with the accumulators at the other locations. This results in the upstream accumulator location having massive vapor generation including severe PDOs, for identical heat fluxes.

3.2.2. Spectral analysis of pressure fluctuations and dependence on vapor generation parameters

Since flow boiling instabilities are inherently associated with periodic pressure fluctuations, temporal P_{in} records (including those presented in Fig. 5) are decomposed into different frequency components using a Fast Fourier Transform (FFT) algorithm in Matlab software. This spectral analysis is performed over a 60-s duration at 200-Hz sampling frequency to generate amplitude, A, ver-

sus frequency, f, plots. It is important not only to characterize flow oscillations by identifying dominant frequencies and peak amplitudes, but also assess how these oscillations are affected by heat flux. These are shown in Fig. 6(a) for the indicated operating conditions and accumulator positions (indicated within the plots). With the accumulator located at 1 (downstream of the test module), oscillations are primarily confined to the range of 3–10 Hz, evidenced by noticeable frequency peaks. The lower heat flux of 54.3 kW/m² does not produce large amplitudes, whereas the intermediate heat flux of 83.0 kW/m² produces larger peaks at frequencies ~7–8 Hz. Higher heat fluxes increase the spread of dominant frequencies, which could be explained by PCI in the heat sink being complicated by interactions between neighboring channels. With the accumulator at location 2 (upstream of the test module), the lower heat flux does not produce any peaks. But both the intermediate and higher heat fluxes produce very clear dominant peaks at ~9–10 Hz, which are associated with a cycle of periodic vapor backflow induced by PDO as already shown in Fig. 3(a). A smaller peak is also produced at ~20 Hz due to stationary flow caused by the confinement of vapor bubble within the channel and vapor stagnation in the inlet plenum; these two phenomena occur during a single cycle of periodic backflow, indicating their frequency should be twice that of the dominant PDO frequency. With the accumulator at location 3 (between the condenser and the pump), oscillations are spread over wider frequency ranges, but with no distinct peaks produced at any heat flux.

To identify the essential non-dimensional parameters that govern pressure oscillations, two parameters that influence vapor generation are investigated: (i) upstream single-phase liquid length and (ii) rate of total vapor generation, which are calculated, respectively, as

$$L_{sp,f} = \frac{GW_{ch}H_{ch}}{q''(W_{ch} + 2W_w)} c_{p,f}(T_{sat} - T_f) \tag{3}$$

and

$$\Delta Q_g = \frac{q''(W_{ch} + 2W_w)N_{ch}(L - L_{sp,f})}{\rho_g h_{fg}}. \tag{4}$$

Here, T_{sat} and T_f are saturation and fluid temperatures, respectively, calculated, along with the fluid properties, at the test module's inlet. Fig. 6(b) provides plots of the peak amplitude of oscillations, A_{max}, versus $L_{sp,f}$ for all operating conditions examined at each accumulator position. For all three positions, A_{max} decreases with increasing $L_{sp,f}$, meaning high G and low q'' tend to suppress the impact of instabilities on pressure fluctuations and even pressure drop. It is interesting that, regardless of the compressible volume location, considerably large amplitudes manifest when $L_{sp,f}$ is between 0.01 and 0.02 m, where stationary liquid flow, bubble clogging, and axial expansion of confined bubbles are observed (see Fig. 3(a)). In other words, at these axial locations, the remaining liquid upstream of the confined bubbles is sufficient for evaporation and the backward evaporative momentum overwhelms the forward liquid inertia with time. As shown in Fig. 6(c), increases in ΔQ_g exasperate the severity of pressure oscillations by intensifying vapor backflow to the inlet plenum. It is noticeable that, for position 2, PDO occurs when total vapor generation exceeds ~4×10^{-5} m³/s.

3.2.3. Pressure drop characteristics

Insights on heat-sink pressure drop, ΔP, characteristics in conjunction with two-phase instabilities for different accumulator positions are obtained by examining the variations of ΔP with other key parameters. Fig. 7(a)–(c) show ΔP variations with heat flux, q'', mass velocity, G, and exit quality, $x_{e,out}$, respectively. Fig. 7(a) shows ΔP increases rather linearly with increases in q'' with a
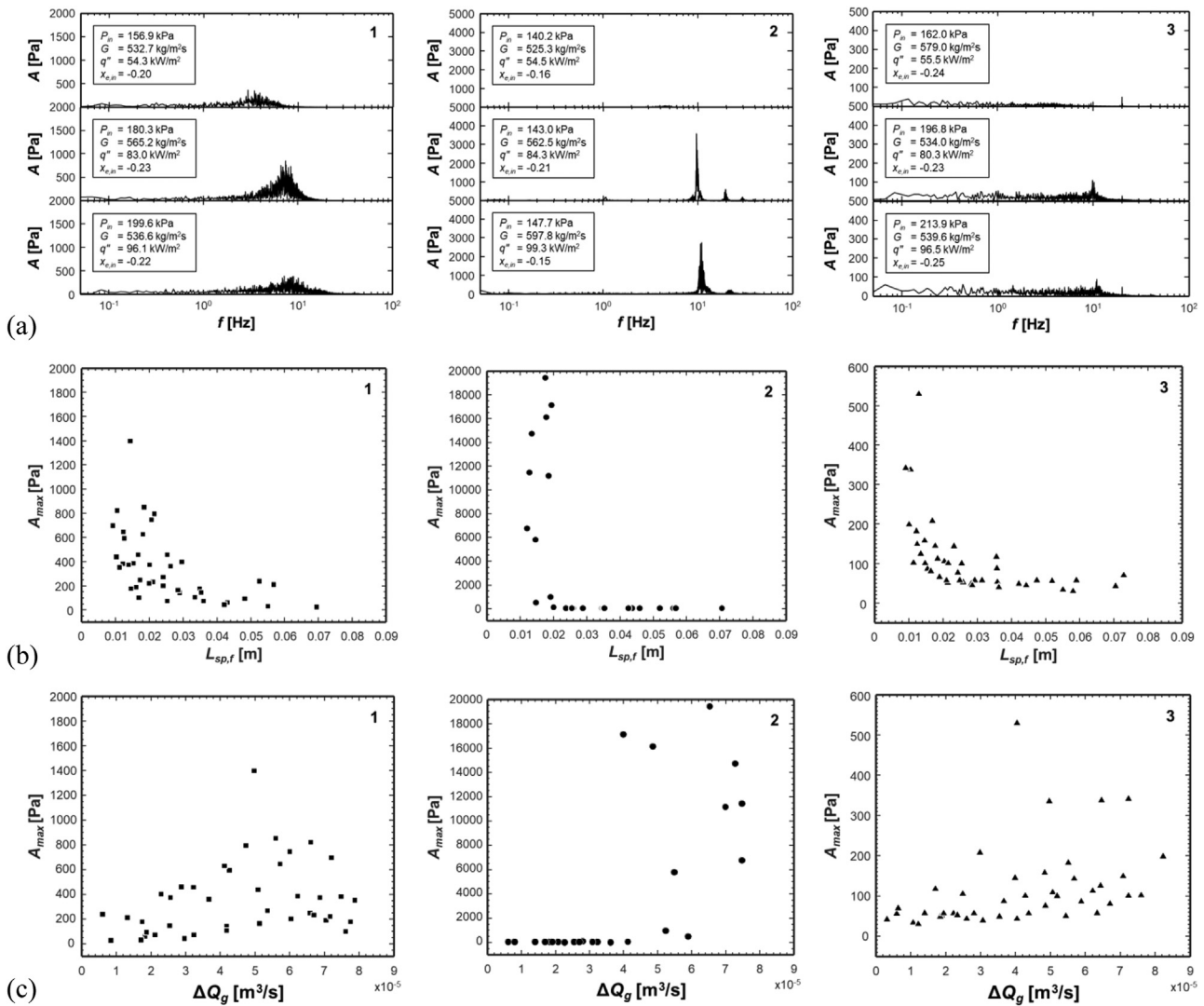
Fig. 6. Assessment of (a) heat flux effects on flow oscillations, and effects of (b) single-phase liquid length and (c) vapor generation parameter on amplitude of two-phase instability for different accumulator positions: 1 = downstream of test module, 2 = upstream of test module, and 3 = between condenser and pump.

slope that decreases with increasing G, the latter being the outcome of two-phase instabilities being more aggressively induced at lower G for a fixed q''. Among the accumulator positions, for identical q'', position 2 induces larger ΔP due to PDO. For several fixed q'' values tested, Fig. 7(b) shows ΔP decreases slightly with increasing G, with a slope that barely changes with changes in q''. This trend with G can be explained as follows. At lower G, flow boiling instabilities (both PDO and PCI) are primarily the result of hydrodynamic oscillations brought about by increases in the rate of evaporation within channels and rapid bubble growth. At higher G, the impact of flow boiling instabilities on ΔP is suppressed due to increases in liquid inertia while frictional ΔP increases. Fig. 7(c) shows ΔP increasing monotonically for most cases with increasing q''. It should be noted that the intuitive increase in ΔP with increasing x_e for fixed q'' is the result of instabilities caused by increased rate of evaporation within channels despite any minor decreases in G.

3.3. Assessment of PDO trends and characteristics

Recall that PCI is the predominant mode of two-phase instabilities when the accumulator is placed at positions 1 (downstream of the heat sink) and 3 (between the condenser and the pump),

with larger fluctuation amplitudes observed with position 1. Additionally, PDO is only observed when the accumulator is at position 2 (upstream of the heat sink) and is associated with severe ΔP oscillations. Compared to PCI, PDO has an appreciable impact on dynamic responses of important parameters as well as system stability. So, instead of focusing on PCI, which has already received much attention in prior works [56], the following will be dedicated to further discussion of oscillations in system parameters resulting from PDO alone.

3.3.1. Temporal records of important test module parameters during PDO

Fig. 8(a)–(c) provide sample temporal plots of the test module's measured inlet and outlet pressures (P_{in} and P_{out}) and temperatures (T_{in} and T_{out}), and local substrate temperatures (T_{tc1} to T_{tc8}, averaged from four thermocouples at the same axial location along the heated length), respectively. The long period presented here includes a near step function increase in heat flux at $t = 0$ s and adjustment of pump speed to overcome the resulting sudden change in mass flow rate. In Fig. 8(a), after the onset of PDO, the amplitude of P_{in} increases until ~1000 s, after which it becomes fairly constant. P_{out} is associated with mild fluctuations, decreases with time, and asymptotically reaches quasi-steady state towards
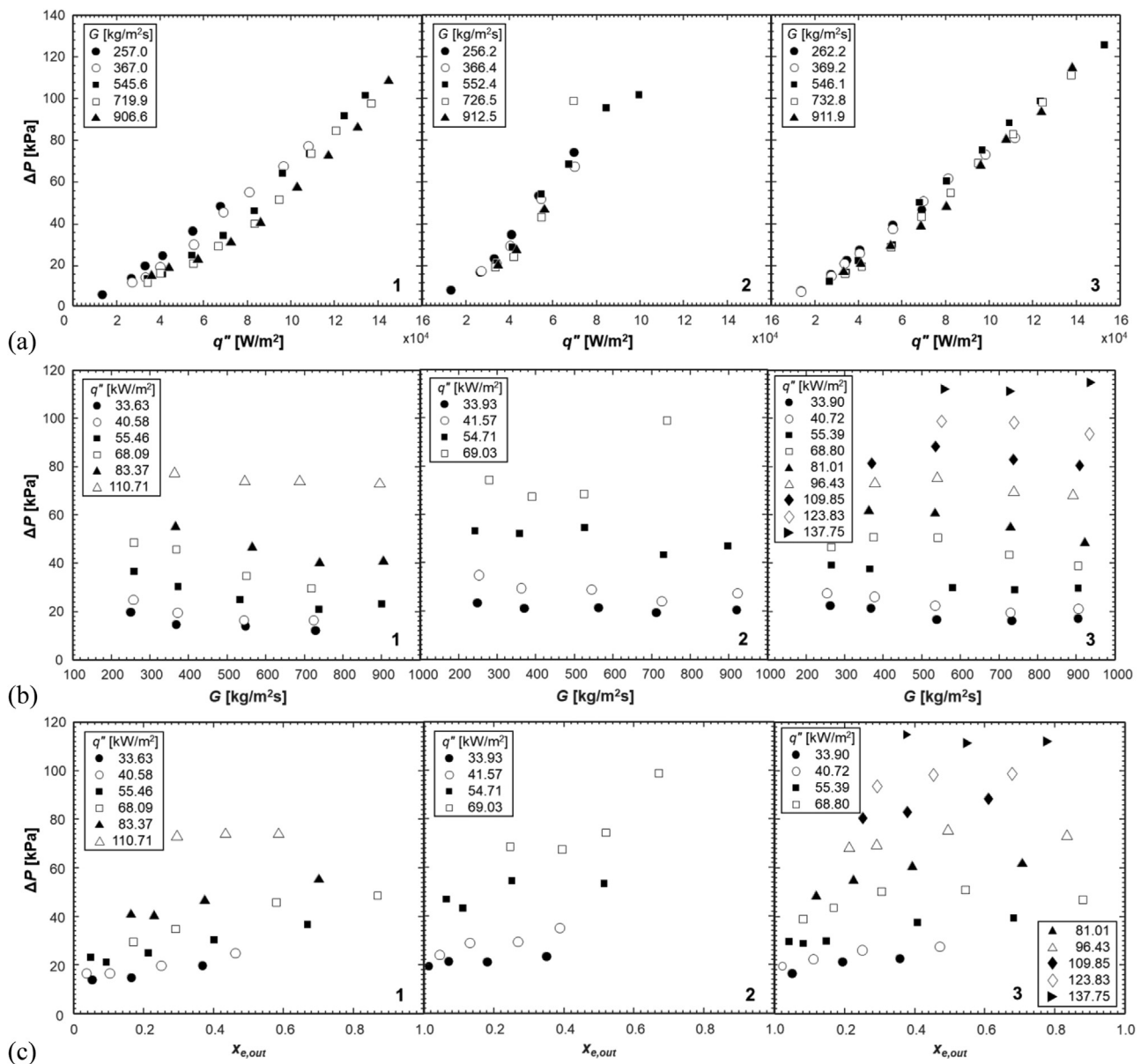
Fig. 7. Variations of pressure drop across micro-channel heat sink with (a) heat flux, (b) mass velocity, and (c) exit quality for different accumulator positions: 1 = downstream of test module, 2 = upstream of test module, and 3 = between condenser and pump.

the end of the period shown. To figure out the oscillatory modes of P_{in} and P_{out}, a narrower 5-s period is examined. Within this short period, P_{in} and P_{out} are 180° out-of-phase, meaning P_{in} values peak when P_{out} decreases to a minimum. Vapor backflow due to vapor bubble confinement raises P_{in} while pressure recovery from expansion is minimum due to the decreasing G. This trend is opposite to one observed in prior studies [56], where P_{in} and P_{out} were reported to fluctuate in-phase. In Fig. 8(b), T_{in} increases logarithmically, meaning operating conditions such as $x_{e,in}$ and $\Delta T_{sub,in}$ change during PDO. On the other hand, T_{out} gradually decreases while mildly fluctuating. Both T_{out} and P_{out} show similar trends with time, this is due to the outlet plenum being mostly at the saturated state.

A unique feature of the present study, because of small thermal mass of the cooper micro-channel heat sink of the present test module, is ability to track local oscillations in wall temperature, which is lacking in prior studies [35,37,40,44,48]. Fig. 8(c) shows temporal record of local heat sink temperatures. Notice that T_{tc1}

and T_{tc2} (measured at $z_1 = 0.5$ and $z_2 = 13.2$ mm, respectively) are lower due to the presence of subcooled liquid and nucleate boiling dominance. Temperature is highest for T_{tc3} (measured at $z_3 = 25.9$ mm) due to bubble clogging and expansion resulting in flow stagnation. T_{tc} is seen to decrease thereafter for a short distance due to convective boiling and flow acceleration, but soon increases again due to liquid deficiency and intermittent dryout.

It was previously shown in the temporal records in Fig. 5 how, among all three accumulator positions, the most significant pressure and mass velocity oscillations were for accumulator position 2. In Fig. 8(a), which corresponds to the same accumulator position, similarly significant pressure oscillations are observed. However, in Fig. 8(c), the wall temperatures are very stable. Note that the resistive heaters supply a constant amount of heat into the test module irrespective of whether instabilities occur or not. With the fluid and wall temperatures being almost constant temporally, the heat transfer coefficient is also almost constant. This is true for all operating conditions in the present study. Therefore, it can
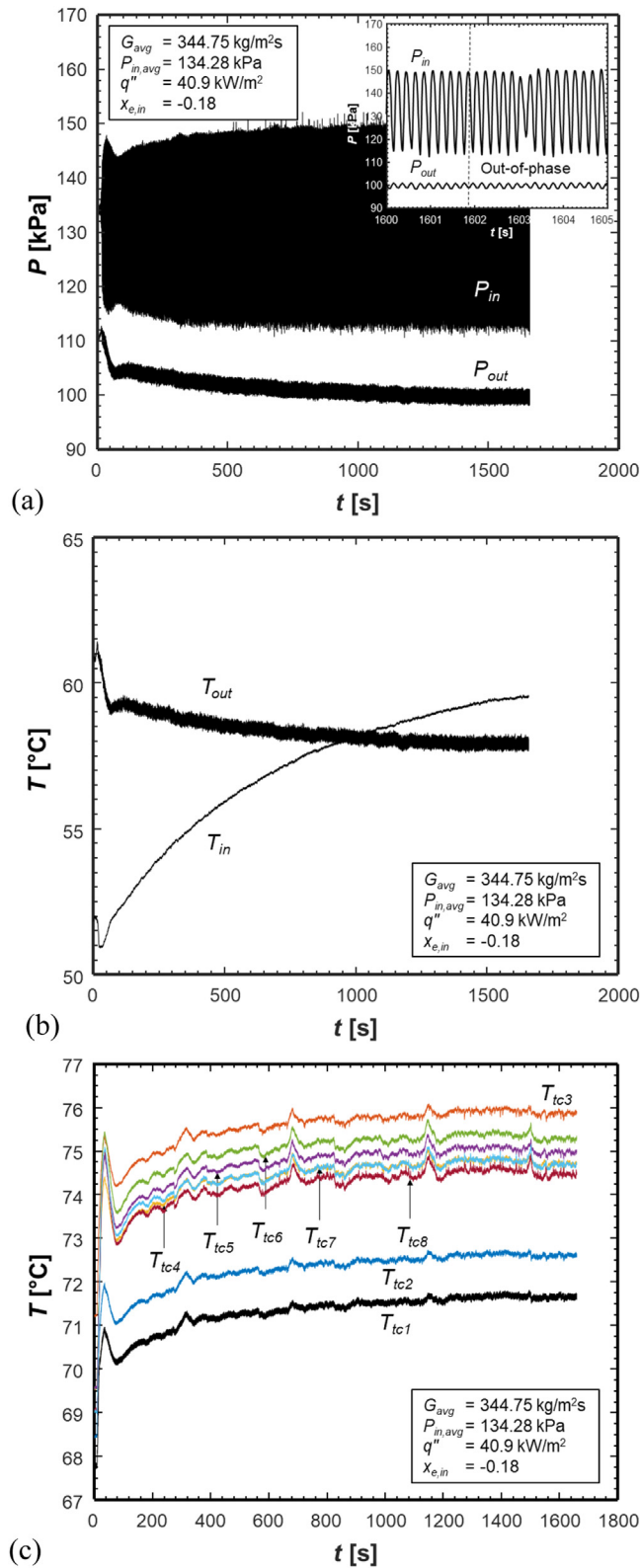
Fig. 8. Sample temporal plots of heat sink's (a) inlet and outlet pressures, (b) inlet and outlet fluid temperatures, and (c) averaged streamwise substrate temperatures for $G_{avg} \approx 350$ kg/m^2 s and $q'' \approx 40$ kW/m^2 corresponding to PDO with accumulator at position 2 (upstream of heat sink).

be asserted that these types of dynamic instabilities do not have any significant effects on heat transfer rates within metallic microchannel heat sinks, nor are they strong enough to induce premature CHF.

3.3.2. Temporal records and spectral analysis of pressures at different flow loop components during PDO

PDO is so severe that the entire system operation deviates farther from the required operating conditions and becomes unstable. Although PDO originates within the heat sink, its effects propagate to other components in the flow loop. Sample temporal records of pressure variations at the pump inlet and outlet ($P_{pump,in}$ and $P_{pump,out}$, respectively) are shown in Fig. 9(a) for the same operating conditions as in Fig. 8. Pressure fluctuations at the module inlet would be felt at all components upstream of the module until the pump outlet, and those at the module outlet would be felt at all components downstream of the module until the pump inlet (see Fig. 2). The $P_{pump,in}$ and $P_{pump,out}$ profiles in Fig. 9(a) match, respectively, the P_{out} and P_{in} profiles in Fig. 8(a) with slight differences. At stable operating conditions, the gear pump continues to discharge liquid by creating a constant pressure differential for a fixed flow rate. But, after the onset of PDO in the heat sink, the pump can no longer maintain the same pressure differential, degrading pump performance. In Fig. 9(b), a single dominant frequency of extremely high amplitude ~17 kPa measured at the module inlet is also evident at the preheater and pump outlet, with higher amplitudes closer to the pump outlet. In Fig. 9(c), a similar trend is observed for other loop locations, except for the amplitudes getting smaller closer to the pump inlet. These trends indicate the difficulty in preventing the propagation of PDO-induced pressure fluctuations away from the heat sink. It can also be seen that the magnitude of oscillations propagating upstream is much greater than that downstream, reflecting the difference present across the test module. Specifically, the preheater pressure is greatly influenced, making it hard to control $x_{e,in}$ for desired heat sink operation.

3.3.3. Techniques to mitigate PDO

Some prior works [28,42,52,61] have investigated techniques to mitigate or even completely eliminate two-phase instabilities. Based on the fundamental understanding of force balance between the liquid and vapor phases developed by Lee et al. [61], modifications to the micro-channel heat sink geometry is a path to increase resistance to vapor expansion to channel upstream. This causes flow reduction or excursion depending on the intensity of vapor generation. The most common techniques in this regard are designing diverging channels and installing inlet restrictions/orifices. Lee et al. [61] tested the effectiveness of both techniques, and although both worked, diverging channels were found to inherently maintain flow stability over wider ranges of operating conditions. Another technique is *valve throttling* to increase system stiffness until the pump outlet pressure increases by a certain value. In Qu and Mudawar's experiments [28], this technique significantly reduced the spatial amplitude of boiling boundary movement in all micro-channels.

To illustrate the effects of valve throttling on PDO, Fig. 10 shows temporal variations of several crucial system parameters. Note that, with the throttling valve upstream of the test module fully open, the system experiences large pressure fluctuations at the beginning. After ~40 s, the valve is half-closed and, as depicted in Fig. 10(a), G decreases roughly by half, which typically magnified instability [56], and the fluctuations are diminished, indicating PDO mitigation. In Fig. 10(b), the amplitude of heat-sink pressure drop fluctuations is diminished from ~35 to ~8 kPa at ~40 s, which is further propagated to the pump as seen in Fig. 10(c), rendering coolant pumping more stable. Due to the stable supply of coolant to the heat sink, PDO mitigation, and better cooling, the substrate
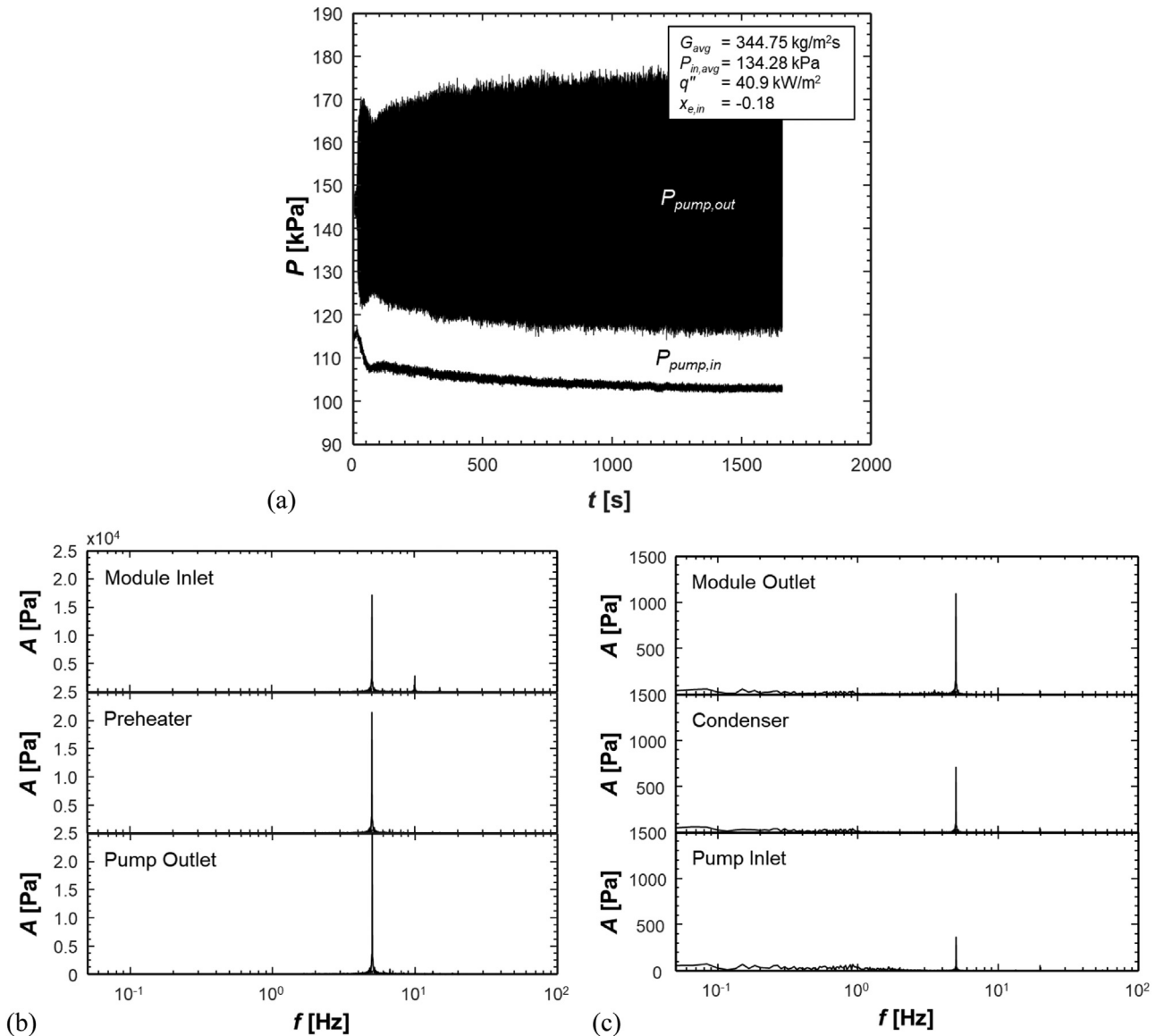
Fig. 9. (a) Sample temporal records of pump inlet and outlet pressures for $G_{avg} \approx 350$ kg/m^2 s and $q'' \approx 40$ kW/m^2, corresponding to PDO with accumulator at position 2 (upstream of heat sink), and spectral analysis of transient pressure signals for loop components (b) upstream and (c) downstream of test module.

temperatures (especially from the middle to the exit) decrease in the period of ~40–260 s (~260 s is when the valve is fully open again) even while PCI persists as seen in Fig. 10(d). As expected, electric power input remains stable, unaffected by what is happening within the loop (see Fig. 10(e)). These observations are similar to those from an earlier work by Cheng et al. [42], who moved the compressible volume to downstream of the test section to eliminate PDO, but PCI (fundamentally induced by DWOs) still persisted. Notice how, once the valve is fully opened again, PDO is reestablished anew, becoming dominant over PCI. G increases back to ~450 kg/m^{2}s with small perturbations at ~270 s, and ΔP fluctuations become severe. This propagates to all other parameters and operation returns to the PDO conditions prior to throttling.

3.3.4. Oscillatory modes of PDO

The PDOs observed in this study have two different oscillatory modes as seen in Fig. 11. Respectively in Fig. 11(a) and (b), short PDO periods of 0.8 and 0.5 s are examined to describe the dynamic behaviors of pressure drop and mass velocity for $G = 252$ kg/m^2 s with $q'' = 40$ kW/m^2 and $G = 562$ kg/m^2 s with $q'' = 84$ kW/m^2.

Due to the flow meter being installed next to the pump, simultaneous changes of G in the heat sink were not captured, but transient flow patterns can still be inferred with the aid of measured G and ΔP during PDO occurrence.

The first oscillatory mode, shown in Fig. 11(a), consists of four transient flow patterns within a periodic cycle. *Sub-period I* is governed by the forward advancement of liquid/vapor mixture from the upstream, accompanied by a G decrease from peak value after bubble nucleation. In the upstream region, a mostly subcooled liquid (mixed with some bubbles from the inlet plenum) enters the channels and undergoes subcooled flow boiling. In the middle of the heat sink, bubbles coalesce and the regime transitions to slug flow. Flow acceleration due to evaporation of saturated liquid, renders the slug flow features deformed and unstable, resulting in increased ΔP. *Sub-period II* experiences flow stagnation due to rapid bubble growth, confinement, coalescence and growth into oblong bubbles, and axial expansion. The increased void fraction greatly increases flow resistance, resulting in flow deceleration to a complete halt, which in turn causes ΔP to significantly decline. *Sub-period III* belongs to the negative-slope portion of the internal char-
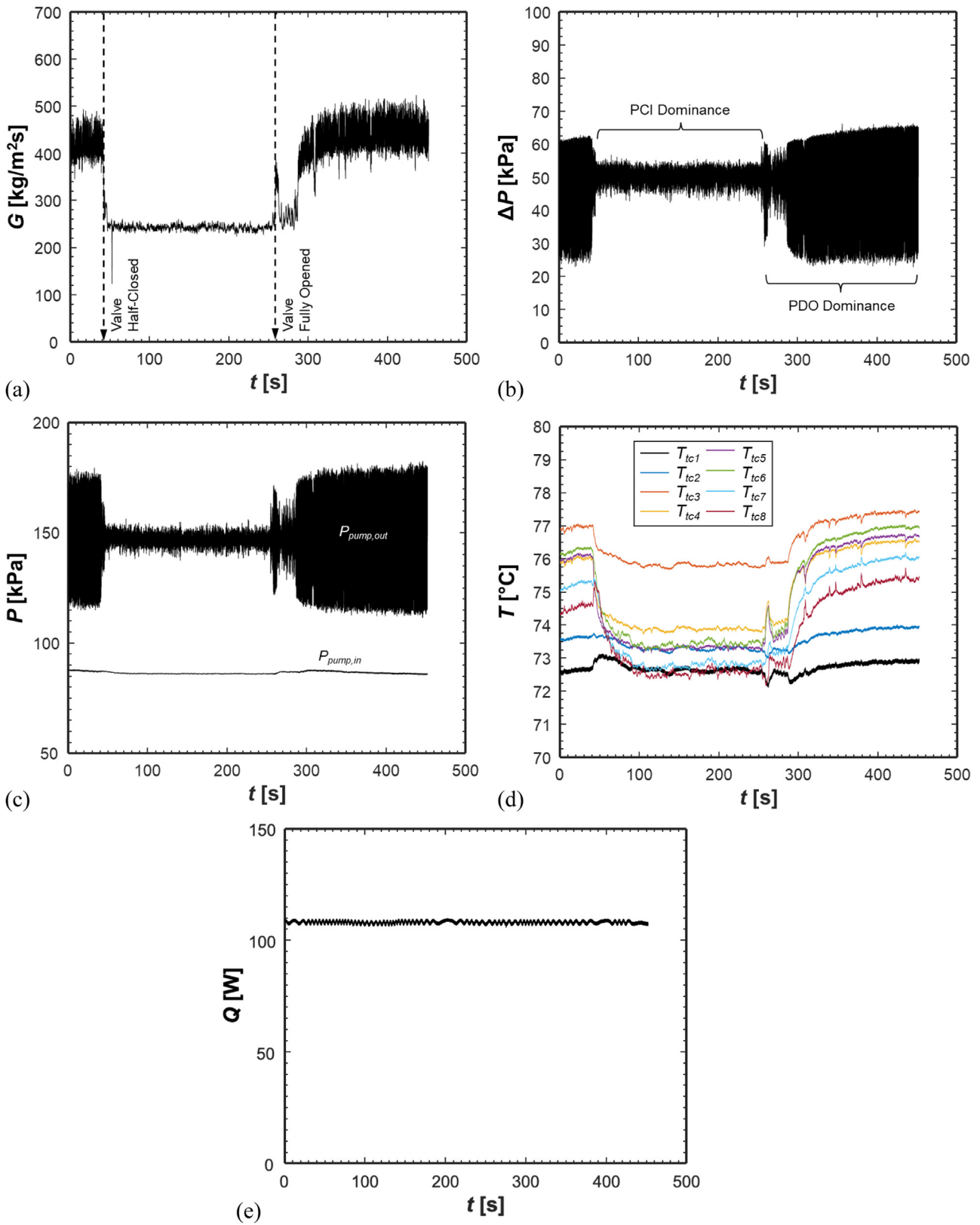
Fig. 10. Effects of valve throttling on PDO, represented by temporal records of (a) mass velocity, (b) heat sink pressure drop, (c) pump inlet and outlet pressures, (d) heat sink substrate temperatures, and (e) heat sink power input.
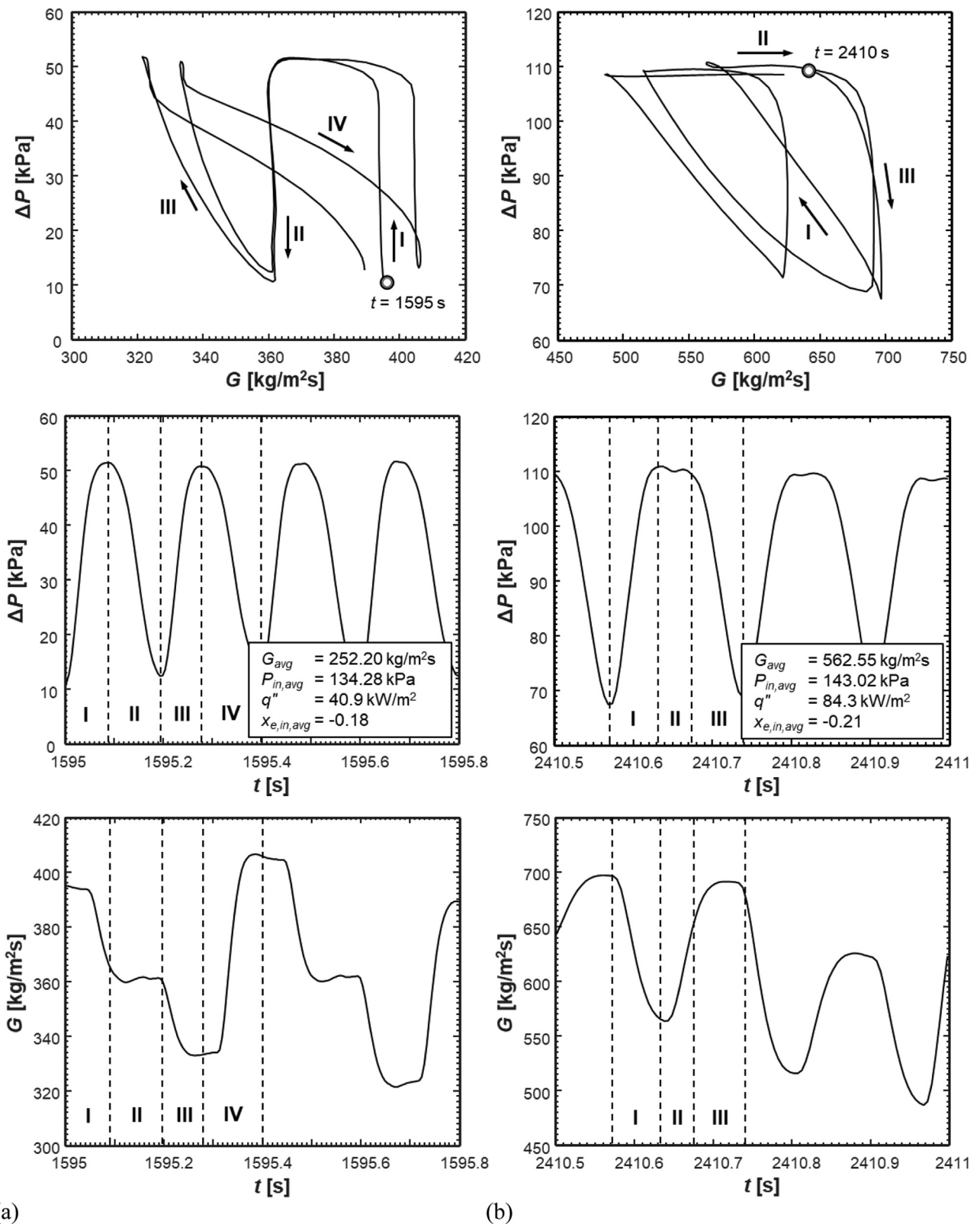
Fig. 11. Oscillations in micro-channel heat sink pressure drop and mass velocity, and pressure versus mass velocity curve during the time period of PDO for two different operating conditions: (a) $G = 252.19$ kg/m^2 s, $q'' = 40.9$ kW/m^2 and (b) $G = 562.55$ kg/m^2 s, $q'' = 84.3$ kW/m^2.

acteristics curve when PDO occurs. Vapor backflow from all channels into the inlet plenum becomes pronounced. This flow reversal increases inlet pressure and ΔP approaches peak value. Stagnated flow causes dryout of the annular film by complete evaporation downstream. *Sub-period IV* marks the resumption of forward flow through the heat sink due to the inlet pressure reaching a peak in the prior sub-period. This not only marks the beginning of G excursion to peak value due to liquid surge at the inlet, but also ΔP to dive to minimum due to a larger amount of liquid flow.

The second oscillatory mode, observed at higher G, consists of three representative sub-periods based on the ΔP versus G plot in Fig. 11(b). Unlike the first mode, G and ΔP oscillate almost 180° out-of-phase, and the period of a single cycle is shorter. *Sub-period I* belongs to the negative-slope portion and is characterized by appreciable bubble nucleation, which leads to bubble confinement, rapid bubble growth, flow deceleration, and ΔP escalation. After the vapor backflow, *sub-period II* begins with a surge of liquid-vapor mixture into the heat sink inlet, causing liquid breakup and droplet shattering. *Sub-period III* begins when subcooled liquid accumulated in the inlet plenum surges through the heat sink following the two-phase mixture, causing ΔP to decrease owing to the much lower frictional and accelerational ΔP components of subcooled-liquid-inlet flow boiling.

3.4. Utilization of stability maps

Prior works [24,33,62] on two-phase instabilities have presented criteria and/or stability maps for predicting the Onset of Flow Instability (OFI) and demarcating stable operating conditions from unstable. It must be emphasized that such maps cannot be universally applied to ascertain the stability of flow boiling because they (i) are formulated for a specific working fluid, test section configuration, and operating conditions, and (ii) oversimplify interdependence of only two parameters in a two-dimensional plot. Nonetheless, they do provide useful foundational framework for use of analysis tools to determine stability boundaries for individual systems, as well as general mechanistic understanding of OFI trends relative to specific dimensionless parameters.

Results of the assessment of stability maps against the present experimental data are shown in Fig. 12(a)–(c) for three pairs of combinations from a set of six dimensionless parameters. The numbers in each plot denote the accumulator location in the flow loop. OFI is indicated by employing a threshold value of 6 kPa for ΔP fluctuations, which has been chosen to segregate stable and unstable operating conditions as done in [46]. It is noted that, even though a certain case is denoted as *unstable* due to minor vapor backflow from some channels into the inlet plenum inducing minor fluctuations slightly over the threshold value, it does not indicate the entire system as being unstable.

The first stability maps shown in Fig. 12(a) are plotted as variations of instability parameter, R, against boiling number, *Bo* ($=q''/(Gh_{fg})$). R is defined as the square-root of the ratio of backward vapor momentum to forward liquid momentum, and is expressed as

$$R = \sqrt{\frac{F_{back}}{F_{forward}}} = \frac{Q}{2Ah_{fg}G}\sqrt{\frac{\rho_f}{\rho_g}}. \tag{5}$$

Lee et al. [61] determined the system becomes unstable when R exceeds unity. For most data points, R increases linearly with increasing *Bo* (albeit some sudden rises in R are seen for position 2), meaning intense vaporization can induce two-phase instabilities. The map shows instability commences for $Bo > \sim 1.1 \times 10^{-3}$, 1.6×10^{-3}, and 2.3×10^{-3} for accumulator positions 1, 2 and 3, respectively, indicating having the compressible volume far away from the test module effectively delays OFI. With the accumulator installed between the condenser and the pump (position 3), flow

states for individual data points are segregated (albeit with some overlap) into stable for $0 < R < 2$, transition for $2 < R < 3.1$, and unstable for $R \geq 3.1$, which show enhanced system stiffness compared to positions 1 and 2.

The second stability map, originally proposed by Bruin and Tadrist [63] and presented in Fig. 12(b), is generated by plotting thermodynamic equilibrium exit quality, $x_{e,out}$, against liquid-only Reynolds number, Re_{fo}. Unlike Bruin and Tadrist's results of clear stability demarcation by a single diagonal line, the present study shows different trends for the 3 accumulation positions. The highly-stable position 3, shows only a few mildly unstable cases, all at low Re_{fo} with high $x_{e,out}$. For position 1, PCI-induced pressure fluctuations over 6 kPa face unstable operation for most saturated outlet conditions. And for position 2, PDO typically manifests at low Re_{fo} with severe pressure fluctuations. Due to an extremely high heat-sink pressure drop for position 2, undesired phase change occurred at the pump entrance, so cases under high Re_{fo} ranges could not be evaluated.

The third instability map, originally proposed by Chang and Pan [46] and shown in Fig. 12(c), is constructed by plotting subcooling number, N_{sub}, against phase change number, N_{pch}, which are defined, respectively, as

$$N_{sub} = \frac{h_f - h_{in}}{h_{fg}}\frac{v_g - v_f}{v_f} \tag{6}$$

and

$$N_{pch} = \frac{Q}{\dot{m}h_{fg}}\frac{v_g - v_f}{v_f}. \tag{7}$$

For accumulator positions 1 and 3, where operating conditions are still manageable during PCI, the data collapse along a horizontal line. For position 1, it is possible to maintain constant inlet subcooling with small fluctuations in both G and system pressure for entire experiment periods even though mild fluctuations over 6 kPa are established at $N_{pch} \approx 32$. For position 2, severe PDO is incurred at a higher N_{pch} of ~ 50 due to massive vapor generation simultaneously from all channels. Note that PDO gradually shifts the operating conditions from the initially-set values, significantly reducing N_{sub} due to vapor backflow.

4. Conclusions

The effects of compressible volume locations in a closed pump-driven flow loop on system instabilities were experimentally investigated for subcooled-inlet flow boiling in a micro-channel heat sink containing 38 parallel channels of 316-µm hydraulic diameter. Three accumulator positions were studied: (1) downstream of test module, (2) upstream of test module, and (3) between condenser and pump. Both high-frequency-sampled temporal parameter data and high-speed video recordings were analyzed for a range of mass velocities and heat fluxes, while inlet subcooling was maintained constant at ~14.5 °C. Key findings are as follows:

(1) Pressure Drop Oscillation (PDO) manifested only with the accumulator located upstream of the test module, whereas Parallel Channel Instability (PCI) remained dominant for the other two locations. System stiffness increases as the accumulator is moved from upstream of the test module to far downstream, effectively suppressing hydrodynamic fluctuations.

(2) PDO was associated with severe, large-amplitude, high-frequency fluctuations in both inlet pressure and mass velocity, culminating in appreciable reversed flow (including vapor backflow to the inlet plenum) simultaneously in all channels. PCI was associated with relatively mild, small-amplitude fluctuations of hydrodynamic parameters. Severe temperature oscillations were not observed with either PDO or PCI. Accumulator gas-side pressure measured at each location along the flow
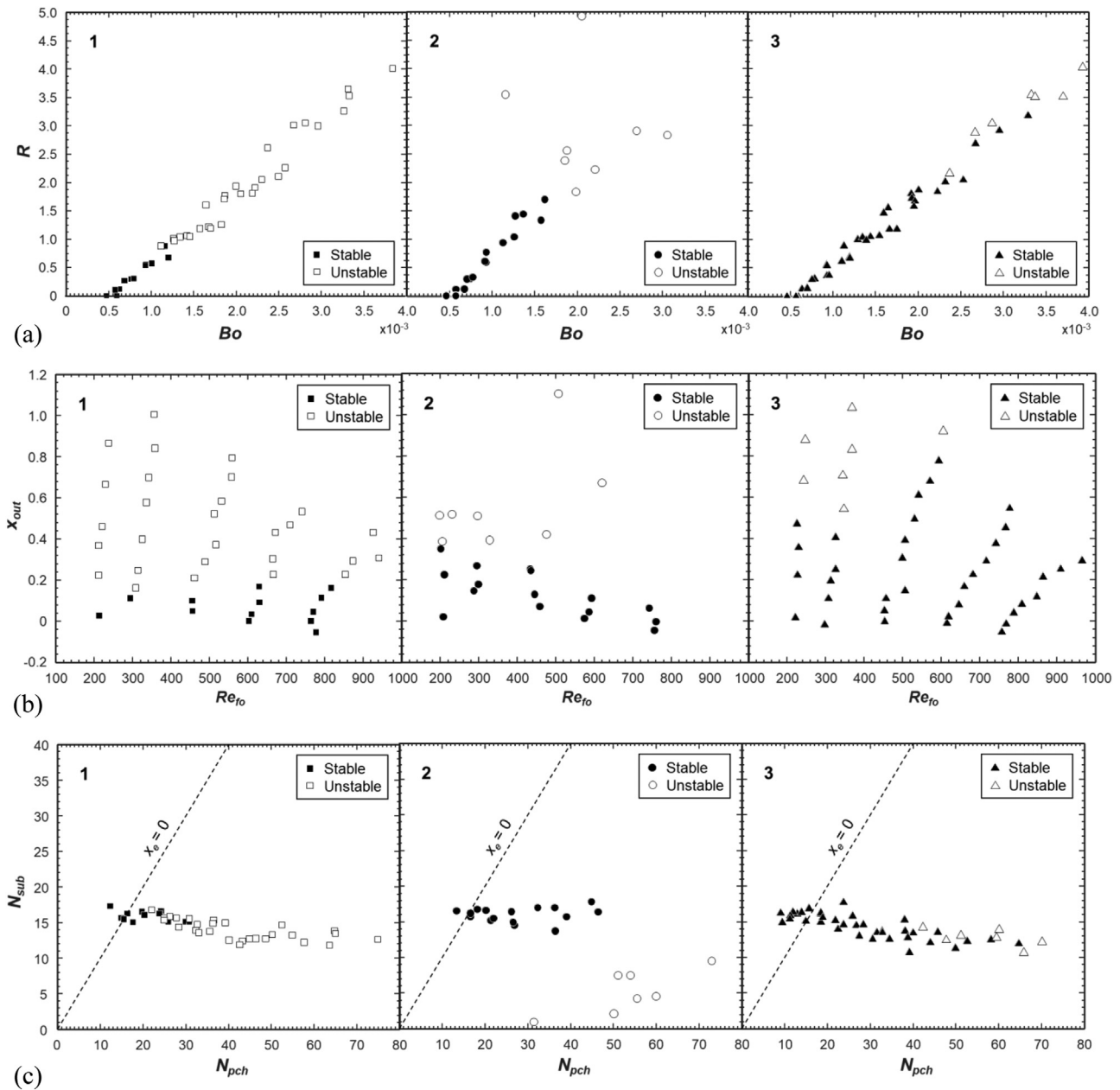
Fig. 12. Assessment of stability maps against experimental data: (a) instability parameter, R, versus boiling number, Bo, (b) thermodynamic equilibrium exit quality, x_{out}, versus liquid-only Reynolds number, Re_{fo}, and (c) subcooling number, N_{sub}, versus phase change number, N_{pch}, for accumulator positioned at 1 = downstream of test module, 2 = upstream of test module, and 3 = between condenser and pump.

loop was stable, performing consistently as a reference point, while instabilities predominantly affected the inlet pressure of the test module.

(3) Flow instabilities resulted in transient flow regimes all along the channel length including bubbly, slug, churn, annular, misty, and even dryout. The instabilities were associated with rapid bubble growth and confinement, elongated bubble growth towards the inlet, and flow reversal, especially for PDO. The channel's downstream region was mainly governed by annular and dryout regimes, the result of massive vapor generation due to flow stagnation and liquid deficiency.

(4) Spectral analysis of pressure signals revealed the dominant frequencies and amplitudes for the different accumulator positions. Vapor generation parameters were also assessed. PDO caused the severe inlet-pressure fluctuations to propagate to all upstream loop components at the same fre-

quency mode, with higher amplitudes closer to the pump exit.

(5) The dynamic instabilities observed in this study did not significantly affect the heat transfer rates, nor did they lead to premature CHF, showing that metallic micro-channel heat sinks are effective for the thermal management of devices requiring high heat dissipation rates.

(6) From a practical system operation point of view, throttling the flow upstream of the heat sink effectively eliminates PDO but renders PCI dominant, and placing the accumulator in the liquid flow segment of the loop between the condenser and the pump ensures the most stable operation.

(7) Existing predictive tools and stability maps were assessed in terms of demarcating stable operating conditions from unstable. All the three stability maps assessed showed the instability criteria to vary for the different accumulator positions, indicat-

ing that a universal two-dimensional map cannot be obtained at the present time, and warranting further study.

Declaration of Competing Interest

The authors declare that they have no known competing financial interests or personal relationships that could have appeared to influence the work reported in this paper.

Data availability

The data that has been used is confidential.

References

[1] L.L. Vasiliev, Heat pipes in modern heat exchangers, Appl. Therm. Eng. 25 (2005) 1–19.

[2] J. Esarte, A. Bernardini, J.M. Blanco, R. Sancibrian, Optimizing the design for a two-phase cooling loop heat pipe, Appl. Therm. Eng. 99 (2016) 892–904.

[3] J. Esarte, J.M. Blanco, A. Bernardini, J.T. San-José, Optimizing the design of a two-phase cooling system loop heat pipe: wick manufacturing with the 3D selective laser melting printing technique and prototype testing, Appl. Therm. Eng. 111 (2017) 407–419.

[4] T.J. LaClair, I. Mudawar, Thermal transients in a capillary evaporator prior to the initiation of boiling, Int. J. Heat Mass Transf. 43 (2000) 3937–3952.

[5] G. Huminic, A. Huminic, I. Morjan, F. Dumitrache, Experimental study of the thermal performance of thermosyphon heat pipe using iron oxide nanoparticles, Int. J. Heat Mass Transf. 54 (2011) 656–661.

[6] G. Liang, I. Mudawar, Review of pool boiling enhancement with additives and nanofluids, Int. J. Heat Mass Transf. 124 (2018) 423–453.

[7] T.A. Grimley, I. Mudawar, F.P. Incropera, Limits to critical heat flux enhancement in a liquid film falling over a structured surface that simulates a microelectronic chip, J. Heat Transf. 110 (1988) 535–538.

[8] T.H. Lyu, I. Mudawar, Statistical investigation of the relationship between interfacial waviness and sensible heat transfer to a falling liquid film, Int. J. Heat Mass Transf. 34 (1991) 1451–1464.

[9] V.S. Devahdhanush, Y. Lei, Z. Chen, I. Mudawar, Assessing advantages and disadvantages of macro- and micro-channel flow boiling for high-heat-flux thermal management using computational and theoretical/empirical methods, Int. J. Heat Mass Transf. 169 (2021) 120787.

[10] C.O. Gersey, I. Mudawar, Effect of heater length and orientation on the trigger mechanism for near-saturated flow boiling critical heat flux II. Critical heat flux model, Int. J. Heat Mass Transf. 38 (1995) 643–654.

[11] M.E. Johns, I. Mudawar, An ultra-high power two-phase jet-impingement avionic clamshell module, J. Electron. Packag. 118 (1996) 264–270.

[12] W.P. Klinzing, J.C. Rozzi, I. Mudawar, Film and transition boiling correlations for quenching of hot surfaces with water sprays, J. Heat Treat. 9 (1992) 91–103.

[13] S. Mukherjee, I. Mudawar, Pumpless loop for narrow channel and micro-channel boiling, J. Electron. Packag. 125 (2003) 431–441.

[14] J. Lee, I. Mudawar, Fluid flow and heat transfer characteristics of low temperature two-phase micro-channel heat sinks—Part 2. Subcooled boiling pressure drop and heat transfer, Int. J. Heat Mass Transf. 51 (2008) 4327–4341.

[15] G. Liang, I. Mudawar, Review of single-phase and two-phase nanofluid heat transfer in macro-channels and micro-channels, Int. J. Heat Mass Transf. 136 (2019) 324–354.

[16] M.K. Sung, I. Mudawar, Single-phase and two-phase heat transfer characteristics of low temperature hybrid micro-channel/micro-jet impingement cooling module, Int. J. Heat Mass Transf. 51 (2008) 3882–3895.

[17] I. Mudawar, Two-phase microchannel heat sinks: theory, applications, and limitations, J. Electron. Packag. 133 (2011) 041002.

[18] H. Zhang, I. Mudawar, M.M. Hasan, Experimental and theoretical study of orientation effects on flow boiling CHF, Int. J. Heat Mass Transf. 45 (2002) 4463–4477.

[19] M.B. Bowers, I. Mudawar, High flux boiling in low flow rate, low pressure drop mini-channel and micro-channel heat sinks, Int. J. Heat Mass Transf. 37 (1994) 321–332.

[20] T. Zhang, Y. Peles, J.T. Wen, T. Tong, J.-Y. Chang, R. Prasher, M.K. Jensen, Analysis and active control of pressure-drop flow instabilities in boiling microchannel systems, Int. J. Heat Mass Transf. 53 (2010) 2347–2360.

[21] M.B. Bowers, I. Mudawar, Two-phase electronic cooling using mini-channel and micro-channel heat sinks: part 1—design criteria and heat diffusion constraints, J. Electron. Packag. 116 (1994) 290–297.

[22] W. Qu, I. Mudawar, Transport phenomena in two-phase micro-channel heat sinks, J. Electron. Packag. 126 (2004) 213–224.

[23] G. Wallace, One-Dimensional Two-Phase Flow, McGraw-Hill, New York, 1969.

[24] L.E. O'Neill, I. Mudawar, Review of two-phase flow instabilities in macro- and micro-channel systems, Int. J. Heat Mass Transf. 157 (2020) 119738.

[25] S. Lee, V.S. Devahdhanush, I. Mudawar, Investigation of subcooled and saturated boiling heat transfer mechanisms, instabilities, and transient flow regime maps for large length-to-diameter ratio micro-channel heat sinks, Int. J. Heat Mass Transf. 123 (2018) 172–191.

[26] K. Balasubramanian, P.S. Lee, C.J. Teo, S.K. Chou, Flow boiling heat transfer and pressure drop in stepped fin microchannels, Int. J. Heat Mass Transf. 67 (2013) 234–252.

[27] J. Lee, I. Mudawar, Critical heat flux for subcooled flow boiling in micro-channel heat sinks, Int. J. Heat Mass Transf. 52 (2009) 3341–3352.

[28] W. Qu, I. Mudawar, Measurement and prediction of pressure drop in two-phase micro-channel heat sinks, Int. J. Heat Mass Transf. 46 (2003) 2737–2753.

[29] A.H. Stenning, Instabilities in the flow of a boiling liquid, J. Basic Eng. 86 (1964) 213–217.

[30] A.H. Stenning, T.N. Veziroglu, Flow oscillation modes in forced-convection boiling, Proc. 1965 Heat Transfer and Fluid Mechanic Institute.

[31] J. Maulbetsch, A Study of system-induced instabilities in forced convection flows with subcooled boiling, Diss. Massachusetts Inst. Technol. (1965).

[32] A.E. Bergles, J.H. Lienhard V, G.E. Kendall, P. Griffith, Boiling and evaporation in small diameter channels, Heat Transf. Eng. 24 (2003) 18–40.

[33] S. Kakac, B. Bon, A review of two-phase flow dynamic instabilities in tube boiling systems, Int. J. Heat Mass Transf. 51 (2008) 399–433.

[34] L.C. Ruspini, C.P. Marcel, A. Clausse, Two-phase flow instabilities: a review, Int. J. Heat Mass Transf. 71 (2014) 521–548.

[35] H.Y. Wu, P. Cheng, Boiling instability in parallel silicon microchannels at different heat flux, Int. J. Heat Mass Transf. 47 (2004) 3631–3641.

[36] Z. Yu, S. Tan, H. Yuan, C. Chen, X. Chen, Experimental investigation on flow instability of forced circulation in a mini-rectangular channel under rolling motion, Int. J. Heat Mass Transf. 92 (2016) 732–743.

[37] S.L. Qi, P. Zhang, R.Z. Wang, L.X. Xu, Flow boiling of liquid nitrogen in micro-tubes: part I—The onset of nucleate boiling, two-phase flow instability and two-phase flow pressure drop, Int. J. Heat Mass Transf. 50 (2007) 4999–5016.

[38] Y. Kuang, W. Wang, J. Miao, X. Yu, R. Zhuan, Theoretical analysis and modeling of flow instability in a mini-channel evaporator, Int. J. Heat Mass Transf. 104 (2017) 149–162.

[39] H. Tuo, P. Hrnjak, Periodical reverse flow and boiling fluctuations in a microchannel evaporator of an air-conditioning system, Int. J. Refrig. 36 (2013) 1263–1275.

[40] L.-J. Guo, Z.-P. Feng, X.-J. Chen, Pressure drop oscillation of steam–water two-phase flow in a helically coiled tube, Int. J. Heat Mass Transf. 44 (2001) 1555–1564.

[41] Y. Ding, S. Kaka, X.J. Chen, Dynamic instabilities of boiling two-phase flow in a single horizontal channel, Exp. Therm. Fluid Sci. 11 (1995) 327–342.

[42] K. Cheng, T. Meng, C. Tian, H. Yuan, S. Tan, Experimental investigation on flow characteristics of pressure drop oscillations in a closed natural circulation loop, Int. J. Heat Mass Transf. 122 (2018) 1162–1171.

[43] I.W. Park, M. Fernandino, C.A. Dorao, On the occurrence of superimposed density wave oscillations on pressure drop oscillations and the influence of a compressible volume, AIP Adv. 8 (2018) 075022.

[44] H. Grzybowski, R. Mosdorf, Dynamics of pressure drop oscillations during flow boiling inside minichannel, Int. Commun. Heat Mass Transf. 95 (2018) 25–32.

[45] S. Lee, V.S. Devahdhanush, I. Mudawar, Frequency analysis of pressure oscillations in large length-to-diameter two-phase micro-channel heat sinks, Int. J. Heat Mass Transf. 116 (2018) 273–291.

[46] K.H. Chang, C. Pan, Two-phase flow instability for boiling in a microchannel heat sink, Int. J. Heat Mass Transf. 50 (2007) 2078–2088.

[47] R. Muwanga, I. Hassan, R. MacDonald, Characteristics of flow boiling oscillations in silicon microchannel heat sinks, J. Heat Transf. 129 (2007) 1341–1351.

[48] M. Wang, M. Zheng, J. Yan, S. Lin, Y. Xiao, Experimental and numerical studies on two-phase flow instability behavior of a parallel helically coiled system, Ann. Nucl. Energy 144 (2020) 107588.

[49] G. Hetsroni, A. Mosyak, Z. Segal, E. Pogrebnyak, Two-phase flow patterns in parallel micro-channels, Int. J. Multiph. Flow 29 (2003) 341–360.

[50] P. Balasubramanian, S.G. Kandlikar, Experimental study of flow patterns, pressure drop, and flow instabilities in parallel rectangular minichannels, Heat Transf. Eng. 26 (2005) 20–27.

[51] J. Xu, J. Zhou, Y. Gan, Static and dynamic flow instability of a parallel microchannel heat sink at high heat fluxes, Energy Convers. Manag. 46 (2005) 313–334.

[52] C.T. Lu, C. Pan, Stabilization of flow boiling in microchannel heat sinks with a diverging cross-section design, J. Micromechanics Microengineering. 18 (2008) 075035.

[53] W. Wang, D. Yang, Z. Liang, M. Qu, S. Ouyang, Experimental investigation on flow instabilities of ultra-supercritical water in parallel channels, Appl. Therm. Eng. 147 (2019) 819–828.

[54] D. Bogojevic, K. Sefiane, A.J. Walton, H. Lin, G. Cummins, Two-phase flow instabilities in a silicon microchannels heat sink, Int. J. Heat Fluid Flow 30 (2009) 854–867.

[55] S. Lee, V.S. Devahdhanush, I. Mudawar, Experimental and analytical investigation of flow loop induced instabilities in micro-channel heat sinks, Int. J. Heat Mass Transf. 140 (2019) 303–330.

[56] J. Lee, S.J. Darges, I. Mudawar, Experimental investigation and analysis of parametric trends of instability in two-phase micro-channel heat sinks, Int. J. Heat Mass Transf. 170 (2021) 120980.

[57] J. Lee, I. Mudawar, Fluid flow and heat transfer characteristics of low temperature two-phase micro-channel heat sinks—Part 1: experimental methods and flow visualization results, Int. J. Heat Mass Transf. 51 (2008) 4315–4326.

[58] R.K. Shah, M.S. Bhatti, Laminar convective heat transfer in ducts, Handb. Single-Phase Convect. Heat Transf. 3 (1987) 1–137.

[59] A. Mukherjee, S.G. Kandlikar, Numerical study of the effect of inlet constriction on bubble growth during flow boiling in microchannels, in: ASME 3rd Int. Conf. Microchannels Minichannels Part B Cont'd, Toronto, Ontario, Canada, ASMEDC, 2005, pp. 73–80.

[60] M.M. Padki, K. Palmer, S. Kakaç, T.N. Veziroğlu, Bifurcation analysis of pressure-drop oscillations and the Ledinegg instability, Int. J. Heat Mass Transf. 35 (1992) 525–532.

[61] H.J. Lee, D.Y. Liu, S. Yao, Flow instability of evaporative micro-channels, Int. J. Heat Mass Transf. 53 (2010) 1740–1749.

[62] L. Tadrist, Review on two-phase flow instabilities in narrow spaces, Int. J. Heat Fluid Flow. 28 (2007) 54–62.

[63] D. Brutin, L. Tadrist, Pressure drop and heat transfer analysis of flow boiling in a minichannel: influence of the inlet condition on two-phase flow stability, Int. J. Heat Mass Transf. 47 (2004) 2365–2377.